# Molecular dimers of methane clathrates: *ab initio* potential energy surfaces and variational vibrational states

| | |
|---|---|
| Journal: | *Physical Chemistry Chemical Physics* |
| Manuscript ID | CP-ART-02-2019-000993.R1 |
| Article Type: | Paper |
| Date Submitted by the Author: | 21-May-2019 |
| Complete List of Authors: | Metz, Michael; University of Delaware, Dept of Physics and Astronomy<br>Szalewicz, Krzysztof; University of Delaware, Dept of Physics and Astronomy<br>Sarka, János; Texas Tech University<br>Tobias, Roland; Eotvos University, Institute of Chemistry<br>Csaszar, Attila; Eotvos University, Department of Theoretical Chemistry<br>Matyus, Edit; Eötvös Loránd University, Institute of Chemistry |

# Molecular dimers of methane clathrates: *ab initio* potential energy surfaces and variational vibrational states

Michael P. Metz,[1] Krzysztof Szalewicz,[1,*] János Sarka,[2]
Roland Tóbiás,[3,4] Attila G. Császár,[3,4] and Edit Mátyus[3,†]

[1]*Department of Physics and Astronomy,*
*University of Delaware, Newark, Delaware 19716*
[2]*Department of Chemistry and Biochemistry,*
*Texas Tech University, Lubbock, Texas, 79409-1061, USA*
[3]*Institute of Chemistry, ELTE Eötvös Loránd University,*
*Pázmány Péter sétány 1/A, Budapest, H-1117, Hungary*
[4]*MTA-ELTE Complex Chemical Systems Research Group,*
*P.O. Box 32, H-1518 Budapest 112, Hungary*

## Abstract

Motivated by the energetic and environmental relevance of methane clathrates, highly accurate *ab initio* potential energy surfaces (PESs) have been developed for the three possible dimers of the methane and water molecules: $(H_2O)_2$, $CH_4{\cdot}H_2O$, and $(CH_4)_2$. While only a single monomer geometry was used for each monomer in the *ab initio* calculations, the PES parameterization makes it possible to produce distinct surfaces for all isotopologues within the rigid-monomer approximation. The PESs were fitted to computations at the frozen-core coupled-cluster level with single, double, and non-iterative triple excitations, employing basis sets of augmented triple- and quadruple-zeta quality plus bond functions, followed by extrapolations to the complete basis set limit. The long-range parts of the PESs are computed using the asymptotic version of symmetry-adapted perturbation theory based on a density-functional description of the monomers. All PESs are polarizable, *i.e.,* in cluster or condensed-phase applications they approximate many-body effects by the induced dipole polarization model. The PESs were developed in a fully automated procedure applying the autoPES method, which is used for the first time to generate near-spectroscopic quality surfaces. The stationary points (SPs) on the PESs have been determined and compared with literature data. For $CH_4{\cdot}H_2O$, previously unknown SPs have been identified and the first detailed study of the $(CH_4)_2$ potential energy landscape has been carried out. The PESs were used in variational quantum nuclear motion computations. The resulting vibrational transitions are in excellent agreement with available high-resolution spectroscopic data. For $(CH_4)_2$, the intermonomer vibrational states are reported for the first time. Analysis of the intermolecular vibrational wave functions in terms of the coupled quantum rotors model highlights a qualitatively different behavior in the intermolecular quantum dynamics of the three dimers.

---

[*] szalewic@udel.edu
[†] matyus@chem.elte.hu

## I. INTRODUCTION

Methane clathrate ($4CH_4 \cdot 23H_2O$), also called methane hydrate, is a solid clathrate compound [1] which holds large amounts of methane in marine sediments [2] and which is thought to be responsible for pipeline blockages during natural gas transportation. In order to better understand the properties of this extended complex, it is necessary to have a model which accurately describes the interactions among the molecular constituents. We have developed intermolecular potential energy surfaces (PESs) for the possible molecular pairs: water-water, methane-water, and methane-methane. This approximation should work well since molecular interactions in methane clathrates are dominated by pair interactions (moreover, these PESs will recover some nondditive effects in a many-body context, see below). The PESs developed during this work for the three dimers will be referred to as WW19, WM19, and MM19, respectively. In addition to getting insights into methane clathrates, our PESs will be valuable in spectroscopic studies of the dimers and possibly multi-mers. In the latter studies, a highly accurate PESs representation is essential as the rovibrational dynamics on the PESs is solved in a practically exact manner. In turn, the most rigorous validation and a possible refinement of a PES is carried out by comparing the computed rovibrational transitions with high-resolution spectra.

Several accurate surfaces have been published for the water dimer [3–15] and the WW19 PES, while it is expected to be on par with best such surfaces, will not further improve agreement with experiment. However, for methane-water only two surfaces have been developed [16, 17] and we anticipate the WM19 PES to be more accurate than the earlier ones. In the case of the methane dimer, the only high-quality PES available is that of Ref. [18] and the MM19 PES should be at least as accurate [although there are no vibrational-rotation-tunneling (VRT) experimental data available yet to provide a stringent, spectroscopic test].

Other potential applications of the PESs developed in the present work include accurate computations of virial coefficients [16, 19]. These quantities are of significance for industry and virials computed with high-quality PESs may replace measured data [19]. Furthermore, the structure and energetics of molecular clusters have always been subject of great interest and the PESs developed in this work will make it possible to accurately predict properties of clusters of essentially arbitrary size, well beyond the reach of *ab initio* computations (as demonstrated in Ref. [20] for water clusters). Another group of applications are studies of properties of liquids, in particular of mixtures of methane and water [21, 22]. As in the case of clathrates, pairwise non-additive interactions are significant in clusters and in condensed phases [23], but they can be well approximated by the polarization model, incorporated into the PESs developed in this study. These PESs, if applied in a many-body environment, will reproduce well many-body polarization effects which dominate pairwise non-additive forces in polar systems or mixtures of polar and non-polar ones [21, 24].

In addition to determining properties of methane clathrates, the water-water, methane-water, and methane-methane interactions are also of fundamental interest on their own. They span the whole range of intermolecular interactions from strong hydrogen bonds, through weak hydrogen bonds, to dispersion-dominated interactions. The water-water interaction, with an interaction energy at the minimum of about $-5$ kcal mol$^{-1}$, epitomizes the case of a strong hydrogen bond. One might think about methane-water as an example for weak hydrogen bonds—at the global minimum configuration with an interaction energy of about $-1$ kcal mol$^{-1}$, the water monomer donates a hydrogen to the carbon atom, whereas at the secondary minimum, only about 30% shallower, methane donates a hydrogen to the oxygen. The authors of Ref. [16] analyzed the physical components of the interaction energy in $CH_4{\cdot}H_2O$ using symmetry-adapted perturbation theory (SAPT) and came to the conclusion that in spite of the geometrical orientations typical of hydrogen bonds, the interactions do not conform well to the textbook characteristics of hydrogen bond interactions which assumes domination by electrostatic forces. On the other hand, the recent IUPAC recommendation for the definition of the hydrogen bond [25] is so broad that these configurations can definitely be considered to represent hydrogen bonds. We also mention a recent study of dimers of alcohols [26], systems that have been considered as typical examples of hydrogen bonding. However, Ref. [26] found that dimers of alcohols such as propanol ot butanol have dispersion interactions comparable with the total interaction energy (*i.e.,* without dispersion these dimers are essentially unbounded). If one interprets this example as ‘an interaction primarily due to dispersion forces’, these dimers would fail the IUPAC definition for hydrogen bonds. Finally, the methane dimer is bound mainly by dispersion forces with the strength of the bond an order of magnitude smaller than that of $(H_2O)_2$, and about two times smaller in magnitude than the interaction of methane and water. Through the spectroscopic study of this series of dimers, one may explore the quantum dynamical fingerprints of the different molecular interaction regimes.

The present status of our knowledge of the three dimers is very uneven. Water pair potentials have a long history [11], many of them have been used in (ro)vibrational computations [3, 8–11, 13, 14, 27–34], and detailed comparisons with high-resolution far-infrared measurement data are available [11, 13, 35]. The $CH_4{\cdot}H_2O$ dimer has been investigated much less thoroughly, either by experiment or theory. Reference [36] reported the only published high-resolution far-infrared spectroscopic data to date, whereas Ref. [37] reported the microwave spectrum of the dimer. There are two qualitatively correct PESs available: an earlier one with rigid monomers [16] and a more recent full-dimensional PES [17]. Both PESs have been used in variational rovibrational computations (also for the deuterated isotopologues) [38, 39]. This work provided the first assignment of the experimental data of Ref. [36]. Very little is known about the quantum dynamics of the methane dimer. The most popular potential for this system was developed by Tsuzuki *et al.* [40] quite some time ago, whereas more recently a much more accurate PES was generated by Hellmann *et al.* [18]. High-level computations were performed recently by Li and Chao [41], but their PES is likely to be not very accurate *(vide infra).* Apparently, no high-resolution far-infrared spectra have been measured for the intermonomer modes, but there are high-resolution observations in the infrared (IR) range [42, 43].

In the present work, we have developed accurate potential energy surfaces for the water-water, water-methane, and methane-methane dimers based on extensive *ab initio* electronic-structure computations. There were a couple of motivations for performing this task. First, we wanted to create a set of PESs for simulations of methane clathrates that are of uniform quality and of uniform functional form, and at the same time their form is simple enough to be used in such simulations. Moreover, the PESs should be of the same quality as the best available ones or better. Finally, the PESs have to be asymptotically correct, since long-range interactions are important for the dynamical study of clathrates. Furthermore, we undertook this project in order to check whether a recently developed automated PES generation method [44] is capable of producing surfaces with an accuracy competitive with the best published ones.

The PESs of this study have been developed using several approximations. First, we assumed that the monomers are rigid: thus, all the potentials are six dimensional (6D). While we could have relatively easily developed flexible-monomer PESs for $(H_2O)_2$ and $CH_4{\cdot}H_2O$, full-dimensional computations of rovibrational states would have been possible only for the $(H_2O)_2$ system. If the flexibility of the monomers is accounted for, the potentials are of significantly higher dimensionality than the 6D rigid-monomer ones: 12D for $(H_2O)_2$, 18D for $CH_4{\cdot}H_2O$, and 24D for $(CH_4)_2$. For $(H_2O)_2$, several 12D potentials exist [5, 6, 10, 12–15, 45, 46]. For $H_2O{\cdot}CH_4$, an 18D potential was recently developed by Qu *et al.* [17]. No 24D PES exists for $(CH_4)_2$, and while development of such a potential is not impossible, it would require an immense computational effort and some compromises in the level of electronic-structure theory and the extent of the basis set. Furthermore, accurate variational (ro)vibrational computations, like those we present here, are currently limited to about 12 degrees of freedom [33]; therefore, such computations cannot be performed with full-dimensional PESs for $(CH_4)_2$ or even for $CH_4{\cdot}H_2O$ at the moment. Thus, the goal of maintaining a uniform treatment of all dimers makes the introduction of the rigid-monomer approximation necessary. This choice also reduces the number of grid points needed to develop the PESs and therefore allows us to use higher levels of theory and larger basis sets. For $(H_2O)_2$, the rigid-monomer approximation performs very well [13, 33] in predicting intermolecular rovibrational modes of the dimer within the energy range explored by far-infrared high-resolution spectroscopy.

The next approximation concerns the level of electronic-structure theory. While the earliest modern PESs for the water dimer were based on SAPT [3–5, 47–51], later on most studies [6, 12, 13, 45, 46] used the coupled-cluster method with single, double, and non-iterative triple excitations [CCSD(T)]. The latter method was applied for the first time to the water dimer in the 1980s [52]. For methane-water, the first modern PES [16] was developed using both SAPT and CCSD(T). For the methane dimer, Tsuzuki *et al.* [40] used the third order of perturbation theory based on the Møller–Plesset partition of the Hamiltonian (MP3), whereas Hellmann *et* *al.* [18] and Li and Chao [41] used CCSD(T). The CCSD(T) method with sufficiently large basis sets is capable to provide interaction energies of closed-shell molecules with uncertainties on the order of 1% relative to the exact solution of the electronic Schrödinger equation within the Born–Oppenheimer (BO) approximation [53, 54].

The CCSD(T) method is also relatively inexpensive compared to other highly accurate methods of treating electron correlation, therefore, for systems like those discussed here one may afford to use relatively large basis sets and perform reliable extrapolations to the complete basis set (CBS) limit. In our work, we were able to use augmented basis sets of triple- and quadruple-zeta quality plus midbond (mb) functions. This is one of the largest basis sets used so far for computations of complete PESs for monomers of the size considered here. The uncertainties of the CBS-extrapolated interaction energies from such bases should be on the order of 1% [53, 54].

There are several further approximations typically made during the development of a PES and also utilized by us: the frozen-core (FC) approximation in CCSD(T) computations, limited sampling of the dimer coordinate space, and a restricted form of the fitting function. We intended to ensure that these approximations introduce errors smaller than those resulting from the use of the CCSD(T) method and of the basis sets specified above.

The outline of this paper is as follows. The *ab initio* methodology used to compute dimer interaction energies is described in Sec. II A, while the subject of monomer geometries is discussed in Sec. II B. The properties of the resulting surfaces are detailed and comparison with literature results is presented in Sec. II C and Sec. II D, respectively. Section III presents the stationary points (SPs) identified on the dimer PESs. Section IV is devoted to the variational computation of the vibrational states of the dimers and their analysis. Sections IV B, IV C, and IV D present vibrational results for the $(H_2O)_2$, $CH_4{\cdot}H_2O$, and $(CH_4)_2$ dimers, respectively. We dedicate Section V to the computation of the $(H_2O)_2$ dissociation energy, a quantity of particular interest due to its recent, accurate measurement [55, 56]. The paper ends in Sec. VI with a summary and conclusions.

## II. POTENTIAL ENERGY SURFACES

As already stated, we have used the CCSD(T) level of electronic structure theory with the FC approximation for all systems at close range, *i.e.,* for separation extending up to about 1.5 times the radial van der Waals minimum separation. The FC assumption is a reasonable approximation at the accuracy level we aim for since the all-electron correction to the FC results is expected to be of the order of 0.5% near van der Waals minima (the effect is 0.5% for the water dimer [57]), *i.e.,* smaller than the uncertainty related to the use of the CCSD(T) method. This level of electronic-structure theory was used in developments of most of the recent high-accuracy PESs for few-atomic monomers. Yet, the FC approximation is likely to be the largest source of uncertainty apart from the truncation of the CC expansion and should be removed in future work. Note that in some of the electronic-structure computations, *e.g.,* in Ref. [58], a hybrid CCSD(T)/MP2 approach (described in detail below) was used. This is a reasonable approach, and it could give results of about the same quality as the present ones with perhaps a somewhat smaller computational effort; nevertheless, we decided to perform the more straightforward direct computations.

The next choice to make is the basis set. For $(H_2O)_2$, the most accurate 6D potential is CCpol-8s of Refs. [9, 24], recently slightly improved in Ref. [20] by including additional grid points on the repulsive wall. At the MP2 level, the *ab initio* calculations in the development of CCpol-8s were performed in Refs. [24, 58] using the augmented correlation-consistent aug-cc-pVTZ and aug-cc-pVQZ basis sets of Dunning and coworkers [59] plus a set of midbond functions and using these two basis sets in CBS extrapolations. Then CCSD(T) energies were computed in the aug-cc-pVTZ plus midbond basis and the CCSD(T)–MP2 correction (both quantities computed in the same basis set) added to the MP2 results. We decided to use the aug-cc-pVTZ and aug-cc-pVQZ plus midbond bases at the CCSD(T) level. Thus, the CCSD(T)–MP2 contribution is more accurate in our work due to the larger basis set and due to the CBS extrapolation. Note, however, that calculations of Ref. [58] correlated all electrons (AE), so in this respect they were more extensive. We will evaluate uncertainties of the various methods in Sec. II D.

Another difference compared to the CCpol-8s computational strategy is the set of grid points at which electronic energies are computed. We have generated a new set of grid points and although this set is smaller than used in Refs. [8, 20, 24], it should lead to an equally accurate PES due the use of a better grid selection algorithm developed Ref. [44]. The form of the fitting function is the same as in Ref. [9], in particular, we have used the optimized off-atomic site locations of CCpol-8s, see Supplementary Information (SI).

The same approach as discussed above for the water dimer was also used for the $CH_4{\cdot}H_2O$ and $(CH_4)_2$ dimers, except that for methane we did not use the off-atomic sites from Ref. [16], but optimized a new set of sites, see SI. Our *ab initio* computations are at least as accurate as any previous ones used in developing complete PESs for any of three dimers considered. In particular, we expect our surface for methane-water to be more accurate than that of Ref. [16] due to the use of a larger basis set and a better sampling of configuration space. It should be also more accurate than the 6D reduction of the 18D PES of Ref. [17], since the latter calculation was not expected to sample well the 6D rigid-monomers space. We therefore expect our WW19 and WM19 PESs to give spectra of similar or better accuracy relative to literature results. For $(CH_4)_2$, no experimental spectra are available, so it will not be possible to evaluate the accuracy of the MM19 PES in this way. The PES of $(CH_4)_2$ computed by Hellmann *et al.* [18] has been obtained at a level of theory similar to that used by us. Another $(CH_4)_2$ potential was developed recently by Li and Chao [41]. They used the same level of theory as we do and basis sets with the cardinal number $X$ larger by one than used by us (however, they did not use midbond functions which are important for the proper description of dispersion interaction [60]). The deviations of their fit from the *ab initio* interaction energies are large, so the overall accuracy of their PES may be compromised by fitting errors.

The autoPES software package [44, 61] was used to automate the generation of the PESs during the present work. A detailed description of the fitting methodology used is included in the SI.

### A. First-Principles Computations

Interaction energies obtained from counterpoise (CP)-corrected [62] supermolecular calculations using the CCSD(T) method in the FC approximation were extrapolated to the CBS limit from the aug-cc-pVTZ and aug-cc-pVQZ [59] plus midbond basis sets separately for the Hartree-Fock (HF) component, $E_{\rm int}^{\rm HF}(X)$, and for the CCSD(T) correlation contribution, $\Delta E_{\rm int}^{\rm CCSD(T)}(X) = E_{\rm int}^{\rm CCSD(T)}(X) - E_{\rm int}^{\rm HF}(X)$, where $X$ denotes the cardinal number of the basis set aug-cc-pV$X$Z plus midbond ($X = 2, 3, 4, \ldots$ corresponds to D, T, Q, ...). The CBS extrapolation formulas followed the scheme recommended in Ref. [63]. For the HF part, we used the $E(X) = E(\mathrm{CBS}) + A\mathrm{e}^{-\alpha X}$ expression with $\alpha = 1.63$, while for the correlation part we used $E(X) = E(\mathrm{CBS}) + BX^{-3}$, where $A$ and $B$ are constants. We used a set of (3s3p2d2f) midbond basis functions placed between the monomers using the so-called $1/R^6$ algorithm of Ref. [64] with exponents given in Ref. [65].

While the interaction energy can be computed for any dimer configuration using the supermolecular method, use of this method to generate data for fitting the entire PES would be needlessly expensive. Thus, we employ a hybrid approach in which supermolecular calculations are performed only at fairly small dimer separations, only up to about 1.5 times the radial van der Waals minimum distance, whereas interaction energies in the asymptotic regime are computed using only monomer properties. Because these asymptotic calculations require a negligible amount of computational effort in comparison to the close-range calculations, the overall computational cost of the PES generation is reduced substantially. The interaction energy in the asymptotic region is computed for a given dimer using a multipole expansion about the centers of mass (COM) of each monomer, as described in Refs. [66] and [67]. Details of the procedure can be found in Ref. [44]. The coefficients of this expansion are computed from monomers' charge density and frequency-dependent density susceptibilities (FDDSs). Ideally, the level of electronic-structure theory used in the asymptotic computations would be identical to that used in the supermolecular calculations, resulting in a seamless connection between the two methods. However, because the asymptotic form of CCSD(T) theory is unknown, monomer charge densities and FDDSs were computed using density functional theory (DFT) in the PBE0 [68, 69] implementation and time-dependent DFT (TD-DFT), respectively. We have applied the gradient-regulated asymptotic correction (GRAC) [70] with ionization potentials of 0.4646 and 0.5164 hartree for water and methane, respectively. Such asymptotics is seamlessly connected with symmetry-adapted perturbation theory based on DFT description of monomers [SAPT(DFT)] [71–79]. This can be seen in Table I, where the SAPT(DFT) and the COM-COM multipole expansion values agree to within 2.6% or better. The intermonomer separation $R$ in Table I is in the intermediate region between the overlap and asymptotic regions (in particular, for $(CH_4)_2$ $R$ is only 1.6 times the minimum value), the agreement would become even better for larger $R$. Table I compares also CCSD(T) and SAPT(DFT) interaction energies, showing that the two approaches are in good agreement at this $R$: the difference in interaction energies is less than 2.6%. Note that the multipole expansion computed using DFT multipole moments and FDDSs reproduces the interaction energy far more accurately in the asymptotic regime than what is possible using supermolecular DFT calculations with semilocal functionals, even when approximate dispersion corrections are included. The COM-COM expansion is subsequently fitted by a distributed expansion, as it is described in SI, and used as a part of each PES fit. This distributed expansion gives values close to those denoted as "PES (undamped)" and differs by 0.02%, 4.8%, and 5.3% from the COM-COM expansion for $(H_2O)_2$, $CH_4{\cdot}H_2O$, and $(CH_4)_2$, respectively (these values include contributions from close-range exponential terms but these terms are are small at this $R$: −0.00043, 0.00185, and 0.00007 kcal/mol, respectively). The relatively lower accuracy in the two latter cases is most likely related to the small number of off-atomic sites used for methane. The PES values with damping, as used in the fits, are also included in Table I, showing that damping is very small at this separation. The relative deviations of the (damped) long-range fit from CCSD(T) values are between 0.3% and 8.5%. The absolute deviations are below 0.004 kcal $\text{mol}^{-1}$, negligible compared to the uncertainties characterizing our methodology. The agreement between all methods listed in Table I is near perfect for $(H_2O)_2$. This is due to the fact that at the separation considered the interaction energy is strongly dominated by the electrostatic component which is easiest to describe. In contrast, for $CH_4{\cdot}H_2O$ the interaction energy is approximately the sum of the electrostatic and dispersion contributions, while in the $(CH_4)_2$ case, it is dominated by the dispersion interaction. The column "PES (undamped)" is given to show that the amount of damping increases as we go from $(H_2O)_2$ to $(CH_4)_2$, which is mainly related to the fact that the van der Waals separation increases in this sequence, so the chosen distance of 6 Å becomes more of near-range type.

### B. Monomer Geometries

The PESs presented here are functions of only the six intermolecular degrees of freedom of the dimers, as the monomer geometries are fixed. This is a good approximation due to the very short timescale of internal monomer vibrational modes relative to the timescale of the intermolecular ones (or timescale of scattering processes).

The question of how to best choose the fixed monomer geometry has been investigated in the literature [80, 81]. A particular choice has a sizeable effect on the global well depth [81] and

TABLE I. Comparison of interaction energies (in kcal $\text{mol}^{-1}$) given by the PESs (damped and undamped) and those using the (undamped) COM-COM asymptotic multipole expansion, SAPT(DFT), and CCSD(T). SAPT(DFT) values were computed up to the second order in the intermolecular interaction operator consistently with the asymptotic ones and used the aug-cc-pVQZ plus midbond basis set in the dimer-centered plus basis set ($\text{DC}^+\text{BS}$) form [60]. All other values are at the same level as in the development of the PESs. All dimer configurations have a COM-COM separation of 6 Å and are at the angular orientation corresponding to the given systems' global minimum using the $\langle r \rangle_0$ monomer geometries.

| System | PES | PES (undamped) | COM-COM expansion | SAPT(DFT) | CCSD(T) |
|---|---|---|---|---|---|
| $(H_2O)_2$ | −0.43155 | −0.43187 | −0.43194 | −0.43223 | −0.43299 |
| $CH_4{\cdot}H_2O$ | −0.06920 | −0.07032 | −0.06711 | −0.06644 | −0.06505 |
| $(CH_4)_2$ | −0.04515 | −0.04612 | −0.04379 | −0.04267 | −0.04160 |

also affects the (ro)vibrational energies [80]. Following the systematic study of Ref. [80], it is recommended to use, instead of the equilibrium geometry commonly used in the literature, the vibrationally-averaged effective structures. Such structures can be obtained from experiments: rotational spectroscopy provides $\langle r^{-2} \rangle_0^{-1/2}$ values, while gas-electron diffraction (GED) measurements give $\langle r^{-1} \rangle_0^{-1}$. Alternatively, one can obtain $\langle r \rangle_v$ values from rovibrational calculations for the $v$th state using an accurate monomer PES. In the present work, we use the computed average values of the bond distances and angles corresponding to the ground-state vibrational wave function of the isolated monomers. These structures will be referred to as the "$\langle r \rangle_0$" structures, where the subscript "0" indicates the ground rovibrational state. Note that the same monomer geometries were used in Ref. [39] to calculate 6D PES values from the 18D PES of Qu *et al.* [17].

The values used by us in the present work, as well as various literature results are listed in Table II. For the water molecule, we used the values computed in Ref. [82] using the highly accurate CVRQD PES [83–85]. For the methane molecule, a regular tetrahedron, the bond length was computed in Ref. [39] using the spectroscopically accurate PES of Ref. [86].

We would like to point out that the differences between the $\langle r \rangle_0$ values and the $\langle r^{-1} \rangle_0^{-1}$ GED values listed in Table II are small but significant: 0.4% for $r$(O-H), 0.2% for $\alpha$(H-O-H), and 1% for $r$(C-H). Still, these differences are generally smaller than the corresponding differences with respect to the $r_{\text{eq}}$ geometries: 1.8%, 0.2%, and 2.2%. The "$\langle r \rangle_0$ molecules" are larger than "$r_{\text{eq}}$ molecules", as it can be expected from the anharmonicity of the potential well. Since reliable theoretical values of $\langle r \rangle_0$ were not available until recently, older PESs used mostly GED values. In particular, for water the GED values of Ref. [87] were used starting from Ref. [81], whereas Ref. [16] used for methane the GED geometry of Ref. [88]. Also note that in most of the literature the GED $\langle r^{-1} \rangle_0^{-1}$ geometries are denoted as $\langle r \rangle_0$ geometries.

We used the atomic masses, $m(\text{H}) = 1.007\,825$ u, $m(\text{C}) = 12$ u, and $m(\text{O}) = 15.994\,915$ u throughout this work, including the variational computation of the vibrational states of the dimers.

TABLE II. Comparison of monomer geometries used (in Å and degrees). For methane, the angle is always the exact tetrahedral angle [$\cos^{-1}(-1/3) = 109.4712206\ldots$] which we entered with machine precision. The $\bar{r}$ geometry is the intermediate geometry used to develop the PESs (see text for further details).

| Monomer | type | $r$(O-H)/(C-H) | $\alpha$(H-O-H) | Reference |
|---|---|---|---|---|
| $H_2O$ | $r_{\mathrm{eq}}$ | 0.95782 | 104.485 | [83–85] |
| | $\langle r^{-1}\rangle_0^{-1}(r_{\mathrm{GED}})$ | 0.9716257 | 104.69 | [87] |
| | $\langle r\rangle_0$ | 0.97565 | 104.430 | [82–85] |
| $D_2O$ | $\langle r\rangle_0$ | 0.97077 | 104.408 | [82–85] |
| $X_2O$ | $\bar{r}$ | 0.97316 | 104.39 | |
| $CH_4$ | $r_{\mathrm{e}}$ | 1.08601 | | [89] |
| | $\langle r^{-1}\rangle_0^{-1}(r_{\mathrm{GED}})$ | 1.09912 | | [88] |
| | $\langle r\rangle_0$ | 1.11002 | | [39, 86] |
| $CD_4$ | $\langle r\rangle_0$ | 1.10446 | | [39, 86] |
| $CX_4$ | $\bar{r}$ | 1.10724 | | |

TABLE III. Interaction energies (in kcal mol$^{-1}$) at the global minimum dimer configuration of the water-methane PES for different monomer geometries. The symbol $CX_4 \cdot X_2O$ indicates the $\bar{r}$ geometries used to generate the PES. In all other cases monomers are in $\langle r\rangle_0$ geometries. See Table II for all monomer geometries. The PESs for the hydrogenic and deuterated monomer geometry cases use the same parameter values as for the $CX_4 \cdot X_2O$ case, so they differ only by the monomer geometries. The angular configuration and COM-COM distance correspond to the global minimum values of the $\bar{r}$ PES.

| System | CCSD(T) | PES | % error |
|---|---|---|---|
| $CX_4 \cdot X_2O$ | −1.04007 | −1.04214 | −0.199 |
| $CH_4 \cdot H_2O$ | −1.04856 | −1.05163 | −0.293 |
| $CD_4 \cdot H_2O$ | −1.03653 | −1.04071 | 0.402 |
| $CH_4 \cdot D_2O$ | −1.04389 | −1.04373 | −0.015 |
| $CD_4 \cdot D_2O$ | −1.03197 | −1.03290 | 0.090 |

We are interested here in both deuterated and non-deuterated forms of the monomers, which differ in their $\langle r\rangle_0$ geometry. The geometries of deuterated species are given in Table II. To compute interaction energies for all ten dimer cases requires ten separate PESs. However, because the geometries of the deuterated and non-deuterated monomers are so similar, we were able to compute accurate interaction energies for all ten cases using only three sets of dimer *ab initio* calculations: one for water-water, one for methane-water, and one for methane-methane. For these calculations, we used monomer geometries halfway between the monomer geometries for the deuterated and non-deuterated cases (defined as the average of the Cartesian coordinates of the atoms, which required in the case of the water molecule to overlay the two molecules such that their centers of mass and the bisectors of angles overlap). Each of the three data sets is used to fit one set of parameters, resulting in three PESs which do not correspond to any of the ten physical cases. The PESs for the ten physical cases can be derived from these three PESs by modifying the monomer geometries while keeping the parameters of the fits fixed. This is possible due to the site-site form of the fit, which is—by construction—appropriate for predicting changes in the PES upon the (small) deformations of the monomer geometry. For large deformations, one can not expect such predictions to be reliable, but for the very small deformations due to deuteration, these predictions are sufficiently accurate, as discussed below. We will refer to the geometry used for the initial fitting of the PES as $\bar{r}$, and the physical deuterated and non-deuterated geometries as $\langle r_{\mathrm{D}} \rangle_0$ and $\langle r_{\mathrm{H}} \rangle_0$ (or simply $\langle r \rangle_0$), respectively.

The implementation of the deformations is obvious if only atomic sites are used in the fit, but requires some further considerations if off-atomic sites are used as well. For the symmetric methane molecule, the change in geometry is determined by a single parameter, *i.e.,* an overall scale factor. Since the off-atomic sites used by us preserve the tetrahedral symmetry, the distances of such sites from the carbon atom are scaled by the same parameter. For water, the displacement of off-atomic sites relative to atomic ones is not unique. An algorithm to generate these displacements was proposed and used in Refs. [5, 15, 90, 91]. In the present work, we had to generalize this algorithm to allow for a more general placement of off-atomic sites optimized in Ref. [9] (not restricted to a vertical plane through the bisector as assumed in the original algorithm). On the other hand, we could exploit the fact that our deformations preserve the $C_{2\mathrm{v}}$ point-group symmetry. Consequently, we used two scale parameters, with the first defining the stretch along the axis from one hydrogen atom to the other and the second defining the stretch along the axis from the oxygen to the midpoint between the two hydrogens. These two scale factors are used to adjust the in-plane coordinates of the off-atomic sites [if the molecule is in the $xy$ plane with the oxygen in the center of the coordinate systems and the symmetry axis along $x$, the $x$ ($y$) coordinate of an off-atomic site is multiplied by the second (first) factor], while the distances from the plane were kept constant. The $\bar{r}$, $\langle r_{\mathrm{H}} \rangle_0$, and $\langle r_{\mathrm{D}} \rangle_0$ geometries for methane and water are given explicitly in the SI.

The accuracy of the procedure described above is illustrated for the case of the global minimum of the methane-water dimer in Table III. In all cases, the error is acceptable as it is below 0.4%, whereas the error of the actually fitted PES at this point is 0.2% and the ratio of the root-mean-square error (RMSE) for negative interaction energies to the depth of the potential at the minimum is 0.95% (see Sec. II C).

### C. Properties of PESs

Interaction energies at each of the global and local minima of the three systems are given in Table IV. There are two symmetry-distinct minima on the $CH_4{\cdot}H_2O$ surface, and a single symmetry-distinct minimum for the other dimers. Symmetry-equivalent minima can be obtained by permutations of hydrogens of the same monomer and exchanging the whole monomers in homogeneous cases. The values computed from the PESs are also included and show that the accuracies of the fits at the minima are satisfactory, with relative deviations smaller than 0.8% and absolute ones below 0.016 kcal $mol^{-1}$. Although such accuracy is inline with the root-mean-square errors (RMSEs) discussed later on, these errors are large relative to typical fits of this type where the interaction energy at the minimum is recovered to several significant digits due to the minimum region being weighted most strongly in the fitting process. This is not the case here due to the fact that the fits were developed for the $\bar{r}$ monomer geometries and then extrapolated to the $\langle r \rangle_0$ geometries.

In order to gain physical insight into the interactions characterizing each minimum, we have performed calculations using SAPT [67, 92]. Unlike supermolecular calculations, SAPT partitions the total interaction energy into physically meaningful components. For a full description of SAPT and definitions of the energy components (electrostatics, exchange, induction, and dispersion), see Ref. [92]. The attractive part of the interaction energy of the water dimer in its minimum configuration is dominated by the electrostatic interaction. This is expected and it is due to water's large permanent dipole moment. The electrostatic interaction is almost completely cancelled by the first-order exchange energy, so that the sum of attractive contributions from the second order is very close to the total interaction energy, although each of these components is three times smaller in magnitude than the electrostatic energy. The ratios of components are quite different for $CH_4{\cdot}H_2O$ at the global minimum. Here the dispersion energy is the largest attractive component. Electrostatics is the second-largest component, but the first-order exchange energy not only cancels this attraction but the total first-order contribution is repulsive. Thus, the methane-water interaction can be considered to be dominated by dispersion forces. At the secondary minimum, the role of dispersion is smaller. This is because the closest contact atoms now include hydrogen and oxygen, whereas in the global minimum a hydrogen atom is close to a carbon and three other hydrogen atoms. Finally, the attractive interaction in the methane dimer, where both monomers have zero dipole and quadrupole moments, is strongly dominated by the dispersion interaction. As in all cases, the first-order exchange repulsion is large and cancels about half of the attractive interaction. The total SAPT interaction energies in the four consecutive rows of the table differ by 3.7%, 9.3%, 2.6%, and 5.1% from the CCSD(T) interaction energies. The SAPT energies are larger in magnitude in three cases which is partly due to the core-valence electron correlation effects included in SAPT.

The errors of the frozen-core approximation used in the development of our PESs are listed in Table V. The correction to the interaction energy in the FC approximation for the water dimer is $-0.033$ kcal $mol^{-1}$, which can be compared to the value of $-0.026$ kcal $mol^{-1}$ obtained by Lane [57], also computed at a high level of *ab initio* theory. The small difference is probably due to the different monomer and dimer geometries used and to the fact the Lane's values are computed using different dimer geometries for the AE and FC cases. The relative importance of the AE–FC correction changes from 0.6% for $(H_2O)_2$, through 1.0% for $CH_4{\cdot}H_2O$, to 0.2% for $(CH_4)_2$.

TABLE IV. Interaction energies (in kcal mol$^{-1}$) at each of the global minima (GM) of the three PESs and for the secondary minimum (SM) in the case of $CH_4{\cdot}H_2O$. The primary components of the SAPT interaction energy are shown: electrostatics, exchange-repulsion, induction, and dispersion. Exact definitions of the SAPT components are given in the SI. The CCSD(T) values are computed at the CBS limit, whereas the SAPT results are computed using the aug-cc-pVQZ plus midbond basis set in the DC$^+$BS form [60]. All values are computed at the $\langle r\rangle_0$ geometry (see Sec. II B).

| System | PES | CCSD(T) | $E^{(1)}_{\text{elst}}$ | $E^{(1)}_{\text{exch}}$ | $E^{(2)}_{\text{indx}}$ | $E^{(2)}_{\text{dispx}}$ | $E^{\text{SAPT}}_{\text{int}}$ |
|---|---|---|---|---|---|---|---|
| $(H_2O)_2$ | −5.1203 | −5.1040 | −8.2128 | 8.0783 | −2.5323[a] | −2.6280 | −5.2948 |
| $CH_4{\cdot}H_2O$ (GM) | −1.0516 | −1.0486 | −0.9028 | 1.6989 | −0.3916 | −1.4011 | −0.9510 |
| $CH_4{\cdot}H_2O$ (SM) | −0.6904 | −0.6961 | −0.7368 | 1.0927 | −0.1974 | −0.8730 | −0.7145 |
| $(CH_4)_2$ | −0.5439 | −0.5467 | −0.2078 | 0.8233 | −0.0064 | −1.1835 | −0.5743 |

[a] Including the $\delta^{\text{HF}}_{\text{int,resp}}$ term, see SI.

TABLE V. Corrections to the frozen-core interaction energies. The interaction energies (in kcal mol$^{-1}$) are computed at the global minima on our PESs using the $\langle r\rangle_0$ monomer geometry. Interaction energies are given with all-electrons correlated and in the frozen-core approximation using the aug-cc-pCV[T/Q]Z basis sets plus the same set of midbond functions as utilized in the calculations of the PESs. The results were then extrapolated to the CBS limit.

| | $(H_2O)_2$ | $CH_4{\cdot}H_2O$ | $(CH_4)_2$ |
|---|---|---|---|
| FC | −5.1033 | −1.0491 | −0.54694 |
| AE | −5.1365 | −1.0595 | −0.54601 |
| AE–FC | −0.0332 | −0.0104 | 0.00093 |

The overall RMSEs of the PESs in different energy regions are shown in Table VI. For each system, a separate set of test data, consisting of 15% of the full data set, was selected randomly and used to evaluate the convergence of the fit (i.e., 85% of the data set was used to fit the PES and 15% was used to test the fit). Once the convergence of the fits was verified, the two data sets were recombined and the full set of $N_{\text{grid}}$ grid points was used to generate the final version of each PES. The value of $N_{\text{grid}}$ varies significantly between the three cases due to the differing number of free parameters. Water requires a more complex fit than methane to achieve the same accuracy, due to its lower monomer symmetry. The regions of the PESs high on the repulsive wall are assigned much lower fitting weights because they are less physically important, and because high fitting errors in this region correspond to a very small shift in the radial location of the repulsive wall. Plots of interaction energies are given as functions of COM-COM separation through each of the local minima of the three dimers in Fig. 1, showing the high quality of the fits.

The final RMSEs in the attractive region are 0.018, 0.010, and 0.006 kcal mol$^{-1}$ for the WW19, WM19, and MM19 PESs, respectively. Relative to the minimum depths, the errors are

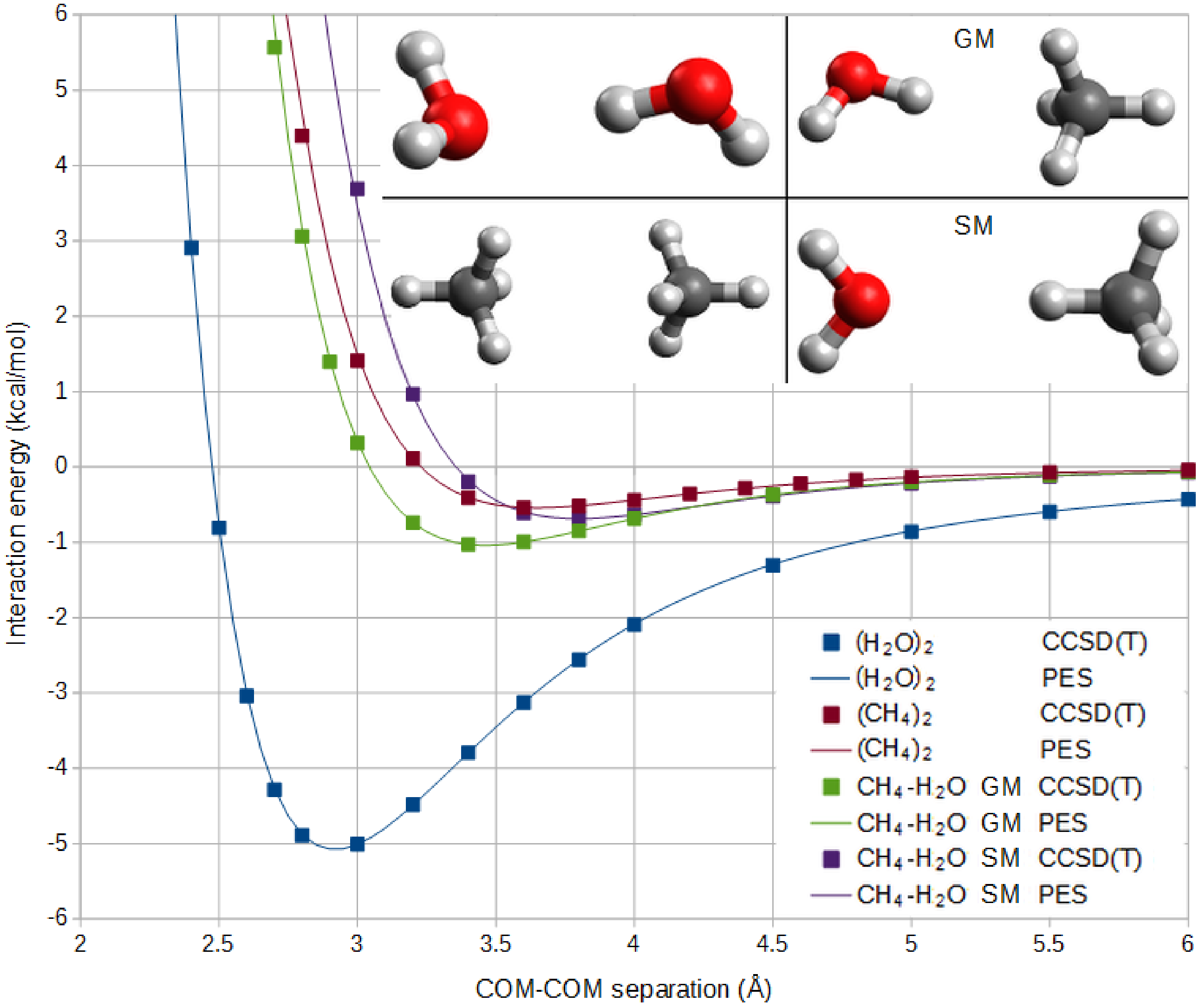

FIG. 1. Interaction energies of $(H_2O)_2$, $CH_4{\cdot}H_2O$, and $(CH_4)_2$ in the $\langle r\rangle_0$ geometry at the orientations corresponding to the global (GM) and secondary (SM) dimer minima configurations (shown in the insert). The symbols denote *ab initio* energies, while the lines are from PESs.

0.36%, 0.95%, and 1.1%, respectively. Thus, while for purposes such as molecular dynamics (MD) simulations of clusters or condensed phases the accuracy is more or less uniform, for applications to dimer spectra the WW19 PES is somewhat more accurate than the other ones. The reason for this nonuniform accuracy is that we have included a relatively small number of off-atomic sites on methane, in fact, only one symmetry-distinct site. If needed, more sites can be added to improve the quality of the fit. What is important is that the fitting errors of the surfaces are considerably smaller than the uncertainties of the *ab initio* calculations. As shown in Sec. II D, in the $(H_2O)_2$ case the latter uncertainties are 0.1 kcal $\text{mol}^{-1}$ or 2%. Thus, the uncertainties of our fit are about a factor of five smaller. It would have been better to have a still more

TABLE VI. RMSEs of the PESs (in kcal mol$^{-1}$). The first three rows show the RMSEs from the last iterations of each fit (performed using 85% of grid points), with RMSEs on testing data sets (15% of grid points) not used in the fits given in parentheses. The number of grid points used in the fit is denoted $N_{\mathrm{grid}}$. The final version of each PES was fit to all data points. The $\bar{r}$ geometry was used in the fitting process.

| System | RMSE for $E < 0$ | RMSE for $E < 10$ kcal mol$^{-1}$ | $N_{\mathrm{grid}}$ |
|---|---|---|---|
| $(H_2O)_2$ | 0.0178 (0.0215) | 0.0499 (0.0523) | 1457 |
| $CH_4{\cdot}H_2O$ | 0.0109 (0.0122) | 0.1578 (0.1438) | 911 |
| $(CH_4)_2$ | 0.0059 (0.0059) | 0.0577 (0.0584) | 269 |
| $(H_2O)_2$ final | 0.0182 | 0.0533 | 1740 |
| $CH_4{\cdot}H_2O$ final | 0.0099 | 0.1176 | 1086 |
| $(CH_4)_2$ final | 0.0060 | 0.0619 | 317 |

TABLE VII. Convergence of interaction energy (in kcal mol$^{-1}$) in basis set size and theory level at the minimum configuration of water dimer. The interaction energies ($U_{\mathrm{min}}$) are computed with respect to the monomer at its equilibrium geometry. All results are from the work of Lane, Ref. [57], unless noted otherwise. DBOC denotes the diagonal BO correction.

| theory level/basis set | $U_{\mathrm{min}}$ |
|---|---|
| CCSD(T)/FC CBS(TQ+mb)[a] | −4.9402 |
| CCSD(T)-F12b/FC CBS(Q5) | −4.9840 |
| plus AE-FC | −5.0103 |
| plus CCSDTQ-CCSD(T) | −5.0184 |
| plus relativistic and DBOC | −5.0208 |

[a] Computed by us using the theory level and basis set of the present work at the geometry in the first column “CCSD(T)-F12b/CBS” of Table 8 in Ref. [57]. All energies are relative to monomers at their isolated-monomer equilibrium geometries taken from the line CCSD(T) and the last two columns of Table 2 in Ref. [57].

accurate fit; however, this would require adding still more off-atomic sites to our fit, while with the current 25 sites (plus the polarization site) the fit is already fairly time consuming to use in MD simulations. Another possibility of increasing the accuracy of the fit would be to use anisotropic site-site functions or include products of isotropic site-site functions. Both options would require modifications of standard MD programs.

### D. Comparison with literature PESs at minima

In order to estimate the uncertainty of our *ab initio* interaction energies, we compare in Table VII the energy computed using our level of theory and basis set with accurate results of Lane [57]. Lane performed calculations at the geometries optimized separately at each level of theory and basis set size, which makes comparisons of convergence of electronic structure

TABLE VIII. Summary of uncertainties of our WW19 PES at the minimum in kcal $\text{mol}^{-1}$ (values in parentheses are in $\text{cm}^{-1}$).

| Source | Uncertainty |
|---|---|
| Incompleteness of basis set | 0.044 (15.3) |
| Frozen-core approximation | 0.033 (11.6) |
| Excitations beyond CCSD(T) | 0.008 (2.8) |
| Relativistic and BODC effects | 0.002 (0.8) |
| Fit | 0.018 (6.4) |
| Extrapolation from $\bar{r}$ to $\langle r\rangle_0$ | 0.014 (5.2) |

methods difficult. However, beyond the CCSD(T)/CBS(TQ) level, the geometry changes are very small and result in completely negligible changes in contributions to interaction energies. Thus, this issue can be ignored. As Table VII shows, at the frozen-core CCSD(T) level the difference between the our and Lanes's result is 0.044 kcal $\text{mol}^{-1}$ or 0.9%. This is the uncertainty resulting from the incompleteness of the basis set used by us. The largest correction to the CCSD(T)/FC interaction energy, accounting for the core-core and core-valence electron correlation, equals 0.026 kcal $\text{mol}^{-1}$ or 0.5%. These observations are in line with those made when discussing Table V, where monomers were taken at $\langle r\rangle_0$ geometries. The correction for higher excitations listed in Table VII is about three times smaller than the AE–FC correction: 0.008 kcal $\text{mol}^{-1}$ or 0.16%, whereas the contributions of the relativistic and diagonal BO corrections are still smaller. Overall, the uncertainty of our *ab initio* interaction energy is only 0.081 kcal $\text{mol}^{-1}$ or 1.6% relative to the exact solution of Schrödinger's equation in the BO approximation. This uncertainty is smaller than one could have expected from general trends, due mainly to a very small contribution from excitations beyond non-iterated triples in this case. It is also possible that there is some accidental cancellation of errors at the minimum. We expect that the relative accuracy will be the same for the WM19 and MM19 PESs. Note that our interaction energy listed in Table VII, $-4.9402$ kcal $\text{mol}^{-1}$, is different from the energy listed in Table IV, $-5.1040$ kcal $\text{mol}^{-1}$, due to differences in the geometries and to the fact that interaction energies computed by us are always vertical (monomers' geometries in the dimer are the same as in isolated monomers), which we will denote as $V_{\text{min}}$, whereas Ref. [57] (and thus the value computed by us and included in Table VII) used interaction energies computed relative to isolated monomers in their equilibrium geometries, $U_{\text{min}}$.

The comparisons with Lanes results [57] allows us to estimate the complete set of uncertainties of our PES for $(H_2O)_2$. Table VIII summarizes such uncertainties at the minimum. The uncertainties due to incompleteness of the basis set, excitations beyond CCSD(T), and effects beyond Schrödinger's equation in the BO approximation are taken from Table VII, those due to the frozen-core approximation from Table V, fitting uncertainty is from Table VI, and the $\bar{r} \to \langle r\rangle_0$ extrapolation one from Table III (assuming the same relative error for $(H_2O)_2$ as for $CH_4{\cdot}H_2O$). The basis set incompleteness error dominates, but the FC approximation error is

TABLE IX. Comparison of geometries (in Å and degrees) and interaction energies (in kcal mol$^{-1}$) at the minimum for $(H_2O)_2$ with literature values. The water internal angle is denoted by $\theta$, $\alpha$ is the angle that hydrogen-bonded O-H makes with the O-O axis, and $\beta$ is the angle between this axis and the bisector of the donor.

| Source | $r_{OH}$ free | $r_{OH}$ donor | $r_{OH}$ acceptor | $\theta$ donor | $\theta$ acceptor | $R_{OO}$[a] | $\alpha$ | $\beta$ | $U_{min}$ | $V_{min}$ |
|---|---|---|---|---|---|---|---|---|---|---|
| CCpol-8s | 0.9716 | 0.9716 | 0.9716 | 104.69 | 104.69 | 2.9105 | 6.0 | 121.88 |  | −5.104[b] |
| HBB2 |  |  |  |  |  |  |  |  | −4.98[c] |  |
| MB-pol |  |  |  |  |  |  |  |  | −4.9599[d] |  |
| CCpol-8sf |  |  |  |  |  |  |  |  |  | −5.02[e] |
| CCpol-8sfIR | 0.9575 | 0.9618 | 0.9590 | 104.71 | 104.67 | 2.9118 | 5.5 | 123.5 | −5.0163 | −5.0285[f] |
| Lane FC |  |  |  |  |  |  |  |  | −4.9840[g] |  |
| Lane | 0.9569 | 0.9641 | 0.9584 | 104.854 | 104.945 | 2.9092 | 5.686 | 123.458 | −5.0208 | −5.0516[h] |
| WW19 $(H_2O)_2$ | 0.97565 | 0.97565 | 0.97565 | 104.430 | 104.430 | 2.9151 | 5.9472 | 121.386 |  | −5.1203[i] |
| WW19 $(D_2O)_2$ | 0.97565 | 0.97077 | 0.97077 | 104.408 | 104.408 | 2.9169 | 5.9661 | 121.467 |  | −5.0363[j] |
| exp/theo[k] |  |  |  |  |  | 2.91±0.005 | 2±4 | 123±10 |  |  |

[a] We use $R_{OO}$ rather than $R$ to conform to literature convention.

[b] Ref. [9]. The *ab initio* and PES interaction energies are identical to the number of digits listed.

[c] Ref. [12], interaction energy from the PES, geometry of minimum not available.

[d] Ref. [14], interaction energy from the PES, geometry of minimum not available.

[e] Ref. [13], value from the PES listed in Ref. [13] to 3 significant digits only.

[f] Ref. [15], values from the PES.

[g] Ref. [57], *ab initio* value at the CCSD(T)/FC level.

[h] Ref. [57], *ab initio* values at the highest level of theory; $V_{min}$ estimated in Ref. [15].

[i] Present work at $\langle r\rangle_0$ geometry of $(H_2O)_2$, the interaction energy given by PES, the *ab initio* value is -5.1040 kcal mol$^{-1}$.

[j] Present work at $\langle r\rangle_0$ geometry of $(D_2O)_2$. the interaction energy given by PES, the *ab initio* value is -5.0573 kcal mol$^{-1}$.

[k] Experimental results [93]. The $R_{OO}$ value was revised in Ref. [50].

similar. Extending the basis set size to quintuple-zeta is possible but would take significant computer resources. Removing the FC approximation is much less costly since calculations even in the aug-cc-pCVTZ basis give converged values for the AC-FC correction. The $\bar{r} \to \langle r\rangle_0$ extrapolation uncertainty can be avoided by performing calculations at the $\langle r\rangle_0$ monomer geometry. Also the accuracy of the fit can be easily improved as discussed elsewhere, but at the costs of loosing compatibility with off-the-shelf MD packages. The remaining two errors are at this point negligible.

In Table IX, we compare the $(H_2O)_2$ geometries and well depths obtained by us with those from the most recent water PESs and with *ab initio* benchmarks. All the depths are within 0.1 kcal mol$^{-1}$ of each other for a given definition of this quantity ($U_{min}$ or $V_{min}$) and part of the discrepancies is due to using different geometries in each case. Thus, theory has reached quite a high level of consistency since not so long ago typical discrepancies between different calculations were closer to 1 kcal mol$^{-1}$. In fact, this current close agreement makes comparisons of results from different papers difficult due to differences in geometries.

Our PES gives a $V_{\rm min}$ value that is 0.016 kcal mol$^{-1}$ below the value from CCpol-8s, the best previous 6D PES for $(H_2O)_2$. The reason for this discrepancy results from uncertainties of the WW19 PES fit, since the *ab initio* computed energies are the same to the number of digits listed. This coincidence of energies happens despite different levels of theory applied and results from a cancellation of two contributions. Our *ab initio* calculations are more accurate than those of Ref. [9] in terms of the basis set, since we used aug-cc-pV(TQ)Z+mb extrapolated results at the CCSD(T) level, whereas Ref. [9] used such extrapolations only at the MP2 level and then added a CCSD(T) correction computed in the aug-cc-pVTZ+mb basis. This difference is expected to make our interaction energy larger in magnitude than that of Ref. [9]. On the other hand, Ref. [9] correlated all electrons, which lowers the interaction energy by 0.03 kcal mol$^{-1}$ compared to the FC approximation used by us. Finally, the monomer geometries used are somewhat different as CCpol-8s uses the GED geometry, as discussed in Sec. II B.

Compared to Lane's $V_{\rm min}$ value at the highest level of theory, amounting to $-5.0516$ kcal mol$^{-1}$, our *ab initio* value of $-5.1040$ kcal mol$^{-1}$ is 0.052 kcal mol$^{-1}$ lower. Here most of the difference results from the use of different monomer and dimer geometries since, as discussed earlier, at the same geometry the difference is 0.081 kcal mol$^{-1}$ and the order of energies is opposite (*i.e.,* the total effect of going from $r_{\rm eq}$ to $\langle r\rangle_0$ geometry is 0.13 kcal mol$^{-1}$, close to the value found in Ref. [81]). As already noted, the use of the $\langle r\rangle_0$ monomer geometry in rigid-monomer approximation leads to much better predictions of properties of water than the use of the $r_{\rm eq}$ geometry.

The $U_{\rm min}$ values from HBB2 and MB-pol are about 0.04–0.6 kcal mol$^{-1}$ above the limit value of Lane and close to the Lane's value at the frozen-core CCSD(T) level, which might indicate that the FC approximation was used during the development of these surfaces (although references [12] and [14] do not mention that this approximation was used). One should point out that HBB2 is not a fully *ab initio* PES. The authors of Ref. [12] used only the aug-cc-pVTZ basis set without midbond functions, which underestimates the magnitude of the interaction energy by at least 0.2 kcal mol$^{-1}$. They computed interaction energies with and without the CP correction (in the latter case getting an overestimation of the magnitude) and then interpolated between these two values to get the benchmark $U_{\rm min}$ from Ref. [94] (which is essentially the same as that from Ref. [57]). The MB-pol result [14] (the value given by the PES from Table 3 of Ref. [14]) is 0.024 kcal mol$^{-1}$ above Lane's [57] value at the frozen-core CBS CCSD(T) level. This difference presumably reflects the error of the MB-pol fit at the minimum, since the authors of Ref. [14] used essentially the same level of theory and basis set as we do, with a minor difference in the midbond basis set.

In Table X, we compare the minima of our methane-water dimer PES to those of the AOSz05 surface from Ref. [16] and of the QCHB15 surface from Ref. [17]. In Ref. [16], several surfaces

TABLE X. Comparison of the van der Waals minima distances ($R$ in Å) and interaction energies (in kcal mol$^{-1}$) for $CH_4 \cdot H_2O$ with literature values. The QCHB15 interaction energies taken from Ref. [17] are presumably $U_{\rm min}$-type quantities while the remaining ones are of $V_{\rm min}$ type.

| Source | $R$ | PES | *ab initio* |
|---|---|---|---|
| Global minimum | | | |
| AOSz05: SAPT PES [16] | 3.49 | −1.01 | −1.03 |
| AOSz05: CCSD(T) PES [16] | 3.51 | −0.97 | −0.99 |
| QCHB15: PES-PI [17] | 3.472 | −1.021 | −1.018[a] |
| WM19 | 3.457 | −1.0516 | −1.0486 |
| Secondary minimum | | | |
| AOSz05: SAPT PES [16] | 3.71 | −0.73 | −0.72 |
| AOSz05: CCSD(T) PES [16] | 3.76 | −0.64 | −0.63 |
| QCHB15: PES-PI [17] | 3.705 | −0.695 | −0.695[b] |
| WM19 | 3.795 | −0.6904 | −0.6961 |

[a] Result without CP correction. The CP-corrected result is −0.944 kcal mol$^{-1}$.
[b] Result without CP correction. The CP-corrected result is −0.638 kcal mol$^{-1}$.

were developed using different levels of theory, with the SAPT and CCSD(T) PESs representing the highest level (the former surface was used in Ref. [38]). The *ab initio* calculations of Ref. [16] applied smaller basis sets than we did (the aug-cc-pVTZ+mb basis set without extrapolations) resulting in the minima at the CCSD(T) level too shallow by about 0.06 and 0.07 kcal mol$^{-1}$ for the global and the secondary minimum, respectively. Since SAPT gives somewhat larger magnitudes of interaction energies at the minima than CCSD(T), cf. Table IV, this effect cancels with the basis set incompleteness error and results in an excellent agreement between SAPT and our CCSD(T) *ab initio* energies: the discrepancies are only 0.02 kcal mol$^{-1}$ for both minima. Reference [16] used a smaller number of off-atomic sites for water than we do, resulting in a somewhat higher fitting error (as seen in Table X). The QCHB15 PES of Qu *et al.* [17] is a true all-dimensional surface (while WM19 is capable of describing intramonomer deformations only to a small degree, see Table III). The QCHB15 PES uses a very different functional form and was fitted to a data set over thirty times larger than that used here. The RMSE of the fit is 0.0097 kcal mol$^{-1}$ for negative interaction energies, similar to our value. QCHB15 is based on energies computed using the explicitly correlated CCSD(T)-F12b method [95] and the aug-cc-pVTZ basis set, but not using midbond functions which are critical for the description of dispersion interactions [60]. Consequently, the CP-corrected interaction energy from Ref. [17] is as much as 0.105 kcal mol$^{-1}$ or 10% above the value computed by us. However, the interaction energies used to construct the QCHB15 PES were not CP corrected. The basis set superposition error (BSSE) of 0.074 kcal mol$^{-1}$ makes the QCHB15 PES closer to the exact one, but one

TABLE XI. Comparison of the van der Waals minima distances ($R$ in Å) and interaction energies (in kcal mol$^{-1}$) for $(CH_4)_2$ with literature values.

| Source | $R$ | PES | *ab initio* |
|---|---|---|---|
| Tsuzuki *et al.* [40] | 3.8 | | $-0.389$ |
| Hellmann *et al.* [18] | 3.633 | $-0.5443$ | |
| | 3.75$^a$ | $-0.5278$ | $-0.5287$ |
| Li & Chao [41] | 3.63 | $-0.475^b$ | $-0.527^c$ |
| MM19 | 3.643 | $-0.5429$ | $-0.5467$ |

$^a$ Values in this row were computed in Ref. [18] for a configuration near the van der Waals minimum.
$^b$ Value read from Fig. 2b.
$^c$ Extrapolated value using the same extrapolation method as in our work.

should keep in mind that BSSE is just a numerical artifact rather than a physical interaction energy component.

In Table XI, we compare the minima of our methane dimer PES to literature values. The most popular potential for this dimer was developed by Tsuzuki *et al.* [40] at the MP3 level using a nonaugmented basis with the size between double of triple zeta. While this was a state-of-art PES at the time of its publication, its minimum is 29% too shallow. A more recent PES of Hellmann *et al.* [18] was fitted to CP-corrected CCSD(T)/FC interaction energies computed in aug-cc-pVTZ and aug-cc-pVQZ bases and extrapolated to the CBS limits. This is essentially the same level of theory that we used (except for midbond functions) and the minimum on the resulting PES is within 0.0014 kcal mol$^{-1}$ of MM19 value, while the COM-COM separations are within 0.011 Å. Both PESs are fit to approximately 300 data points and the functional forms of the fits are also quite similar, although our form is somewhat more elaborate. Differences between the two PESs include different choices of grid points and different fitting methodology. The authors of Ref. [18] did not compute the *ab initio* energy at the minimum of their PES, therefore we give in Table XI their values for a near-equilibrium configuration showing that the quality of their fit is excellent. Another difference between the two PESs is that we use here the *ab initio* computed C-H bond length of 1.11002 Å, whereas in Ref. [18] an experimental value of 1.099 Å was used. The $(CH_4)_2$ potential of Li and Chao [41] is fit to CCSD(T) interaction energies extrapolated from the aug-cc-pVQZ and aug-cc-pV5Z basis sets. The monomer geometry has C–H $r_{\rm eq}$ separation of 1.085 Å. These authors do not specify if they used the FC approximation. Their extrapolated interaction energy is quite far (0.02 kcal mol$^{-1}$) from our value, which is probably due to their use of the equilibrium monomer geometry. As we argued earlier, this is not an appropriate choice for a rigid-monomer PES. An even larger source of uncertainty for the Li-Chao PES is their use of an exceedingly simple fitting function, containing only six free parameters. As seen in Table XI, the fit error at the equilibrium is about 0.05 kcal mol$^{-1}$, much

TABLE XII. Comparison of the $(H_2O)_2$ dimer stationary points on the WW19 PES at the $\langle r \rangle_0$ monomer geometry with literature results. The barriers, $E$, relative to the global minimum are given in $cm^{-1}$. 'Rank' indicates the number of negative eigenvalues of the Hessian at the stationary point.

| WW19 PES | | | CCpol-8s | Refs. [9, 94][a] | Ref. [94] |
|---|---|---|---|---|---|
| # | Rank | $E$ | $E$ | $E$ | $E$ |
| 1 | 0 | 0.0 | 0.0 | 0 | 0 |
| 2 | 1 | 189.37 | 190.5 | 189 | 181± 5 |
| 3 | 2 | 202.38 | 212.6 | 212 | 198± 6 |
| 4 | 1 | 265.58 | 250.0 | 252 | 245±15 |
| 5 | 1 | 370.09 | | | |
| 6 | 2 | 370.09 | 342.4 | 344 | 333±15 |
| 7 | 3 | 387.74 | 368.2 | 364 | 348±18 |
| 8 | 1 | 708.76 | 701.0 | 711 | 625±16 |
| 9 | 2 | 709.05 | 702.4 | 693 | 634±18 |
| 10 | 3 | 1023.50 | 1027.0 | 1028 | 948±23 |
| 11 | 3 | 1303.32 | 1293.6 | 1309 | 1249±21 |
| 12 | 2 | 1948.59 | | | |
| 13 | 3 | 1983.97 | | | |

[a] We subtracted the monomer deformation corrections of Ref. [9] from the fully-dimensional values of Ref. [94] for a better comparison with the present rigid-monomer results.

larger than the uncertainty of the underlying *ab initio* approach which is likely below 0.01 kcal $mol^{-1}$ relative to the exact BO value.

## III. STATIONARY POINTS

Table XII lists stationary points of the $(H_2O)_2$ dimer. The SPs are ordered by energy as obtained for the WW19 PES, so the numbering is different from the classic ordering of Smith *et al.* [96]. We compare the WW19 PES barriers with the most accurate literature values: the CCpol-8s PES [9] and direct optimization on an *ab initio* surface by Tschumper *et al.* [94]. The stationary points from the different searches are correlated based on their energy, geometry, and the number of negative eigenvalues of the Hessian at that point.

The optimizations by Tschumper *et al.* [94] were performed in 12 dimensions, so their barriers include contributions from monomer deformations, Such optimizations result in near-equilibrium monomer geometries at SPs on the full-dimensional surface. Cencek *et al.* [9] computed monomer distortion corrections to their six-dimensional treatment. We have used these corrections and subtracted them from the full-dimensional values of Ref. [94]. These 'rigidized' barriers will serve as the benchmarks for the present work. The SP barriers of the WW19 PES have an RMSE of 14 $cm^{-1}$, with the largest deviation 26 $cm^{-1}$, relative to the benchmark. All but three barriers are within error bars of the benchmark values. The CCpol-8s barriers are somewhat closer to the

TABLE XIII. Comparison of the $CH_4{\cdot}H_2O$ dimer stationary points on the WM19 PES at the $\langle r\rangle_0$ monomer geometry with literature results. The barriers, $E$, relative to the global minimum are given in $\mathrm{cm}^{-1}$. 'Rank' indicates the number of negative eigenvalues of the Hessian at the stationary point.

| WM19 PES | | | Ref. [97] |
|---|---|---|---|
| # | Rank | $E$ | $E$ |
| 1 | 0 | 0.00 | 0.0 |
| 2 | 1 | 3.06 | 2.8 |
| 3 | 1 | 70.41 | 76.0 |
| 4 | 2 | 82.53 | |
| 5 | 1 | 108.36 | |
| 6 | 2 | 108.70 | |
| 7 | 1 | 126.33 | 131.9 |
| 8 | 2 | 126.44 | |
| 9 | 2 | 131.59 | |
| 10 | 2 | 166.40 | |
| 11 | 3 | 170.49 | |
| 12 | 3 | 248.74 | |
| 13 | 2 | 254.23 | |
| 14 | 2 | 291.37 | |
| 15 | 3 | 294.07 | |
| 16 | 3 | 299.03 | |
| 17 | 2 | 306.36 | |
| 18 | 3 | 306.37 | |
| 19 | 3 | 309.00 | |
| 20 | 4 | 309.88 | |
| 21 | 4 | 319.84 | |
| 22 | 4 | 352.69 | |
| 23 | 5 | 352.86 | |
| 24 | 5 | 369.92 | |
| 25 | 6 | 369.94 | |

benchmark with a 7 $\mathrm{cm}^{-1}$ RMSE. A possible reason for the larger RMSE of the present results is the $\bar{r}$ to $\langle r\rangle_0$ extrapolation used in the WW19 PES.

We obtained three SPs not observed before. The new points #12 and #13 are above the dissociation asymptote, *i.e.,* correspond to positive interaction energies. Earlier work might have been limited to the negative region. The apparently 'new' point, #5, is most likely due to an artifact of the WW19 PES. SP #5 and #6 have almost identical energies, same to all digits shown in the table, and the root-mean square deviation (RMSD) between the geometries of these points is on the order of 0.001 Å (0.001 Å difference in $R$ and less than 2 degrees in the Euler angles). We examined this region of the PES very closely: there is an almost flat (with ca. 0.1 $\mathrm{cm}^{-1}$ variations in the energy), very narrow, and crooked valley connecting SP #5 and #6. This wrinkle in the PES is at least an order of magnitude smaller than the accuracy of the fit, which has an RMSE of 0.018 kcal $\mathrm{mol}^{-1}$ (6.3 $\mathrm{cm}^{-1}$).

Table XIII lists SPs for $CH_4{\cdot}H_2O$. We have found 25 SPs (including the global minimum) on WM19 PES. For this dimer, the literature data are very limited, we compare the results with those of Rivera-Arrieta *et al.* [97] who performed full-dimensional searches at a high-level of electronic structure of theory. The agreement is reasonably good (remember that in a fully-dimensional search the monomers relax to a near-equilibrium monomer geometry). The first barrier (SP #2, 3.06 $\text{cm}^{-1}$) is very low. The existence of such a low barrier can be understood by following a pathway which connects it with the global minimum. In the global minimum structure, one of the O-H bonds points into the middle of the pyramid formed by C and three H atoms. The water molecule is in the plane formed by C and two of methane's H's and the other O-H is approximately parallel to one of the C-H bonds in the plane (see Fig. 1). To arrive at SP #2, one needs to rotate water 180° around the 'hydrogen bond' (this point can also be reached by rotating methane 120° around this bond). The resulting configuration is energetically very close to the global minimum since the only difference comes from the interaction of the fairly remote free H with the H atoms of methane. A further 180° rotation gets back into the global minimum. For comparison, SP #5 with 108 $\text{cm}^{-1}$ barrier, is obtained if the water molecule is rotated in plane around C, keeping O-H pointing into C, until it points between the two methane hydrogens that are in plane. In this case, the environment of the 'bonding' hydrogen changes quite significantly.

We observe on the WM19 PES similar 'double features' as on the WW19 PES, which probably indicate that both surfaces have unphysical wrinkles, but in both cases these wrinkles are much smaller than the estimated accuracy of the PESs (and hence the accuracy of the vibrational transitions). It is known that $CH_4{\cdot}H_2O$ has a secondary minimum (SM) [16, 97]. We can identify the SM with SP #7, which is 126.33 $\text{cm}^{-1}$ higher in energy than the global minimum. Note that SP #7 is labelled in the table as a first-order saddle point ('rank' is 1). By looking at the eigenvalues of the Hessian, we may observe that its only negative eigenvalue is near zero and probably beyond the accuracy of the numerical derivatives of the surface. Thus, based on earlier evidence, we accept this point as the SM and remember that the SM valley is extremely flat and shallow.

Table XIV lists SPs for $(CH_4)_2$. We found 17 SPs on the MM19 PES. Since we are not aware of any literature references regarding the topology of the $(CH_4)_2$ surface, no comparisons are possible. The lowest barriers are smallest among the three dimers (except for the 3 $\text{cm}^{-1}$ barrier in the case of $CH_4{\cdot}H_2O$), which is simply related to the interactions being weakest for $CH_4{\cdot}H_2O$. As for other dimers, we observe a few 'double features', probably due to small, unphysical wrinkles on our PES.

## IV. VIBRATIONAL NUCLEAR MOTION COMPUTATIONS

The best way to test the quality of a PES is to use it in variational nuclear-motion computations and compare to spectral measurements. Thus, the present paper reports vibrational results for $(H_2O)_2$, $CH_4{\cdot}H_2O$, and $(CH_4)_2$. For all three dimers, we use a six-dimensional model for the PESs and carry out vibrational computations similar to earlier work on molecular dimers

TABLE XIV. Stationary points of the $(CH_4)_2$ dimer on the MM19 PES at the $\langle r\rangle_0$ monomer geometry. The barriers, $E$, relative to the global minimum are given in $cm^{-1}$. 'Rank' indicates the number of negative eigenvalues of the Hessian at the stationary point.

| MM19 PES | | |
|---|---|---|
| # | Rank | $E$ |
| 1 | 0 | 0.0 |
| 2 | 1 | 15.65 |
| 3 | 2 | 15.81 |
| 4 | 3 | 17.71 |
| 5 | 1 | 26.07 |
| 6 | 2 | 30.13 |
| 7 | 2 | 32.73 |
| 8 | 3 | 33.99 |
| 9 | 2 | 36.23 |
| 10 | 3 | 36.39 |
| 11 | 2 | 40.89 |
| 12 | 3 | 58.91 |
| 13 | 3 | 69.32 |
| 14 | 4 | 69.32 |
| 15 | 4 | 75.18 |
| 16 | 4 | 125.56 |
| 17 | 5 | 125.64 |

[3, 9, 11, 27, 28, 31, 98]. However, this time we use the general rovibrational program, GENIUSH [99, 100], as in Refs. [38, 39]. The six-dimensional vibrational model assumes rigid monomers and describes the intermonomer configurations using the distance between the centers of mass of the monomer units, $R$, and five angular coordinates $(\cos\theta, \phi, \alpha, \cos\beta, \gamma)$, as defined in Ref. [38]. The monomer geometries are held fixed at the effective $\langle r\rangle_0$ structures of the monomers (see Table II) during the rovibrational computations by using the rigorous reduced-dimensionality approach intrinsic to the GENIUSH program [99]. Note that other rigid-monomer structures are considered in relation with the calculations of dissociation energies (see Sec. V).

### A. Solution of the nuclear Schrödinger equation

Hereby we report benchmark-quality vibrational energies for the newly developed WW19, WM19, and MM19 PESs described in Section II. Peculiarities of the intermolecular vibrational dynamics, rovibrational states, and a detailed wave function analysis will be presented in a forthcoming publication [101].

The time-independent vibrational Schrödinger equation was solved by calculating the lowest-energy states of the Hamiltonian matrix using an iterative Lanczos eigensolver [99, 102]. The matrix representation of the Hamiltonian is constructed using the discrete variable representation (DVR) within a direct product basis and grid for the six vibrational degrees of freedom. Basis function types, the number of grid points, and the intervals are given in Table XV for the most

TABLE XV. Internal coordinates (Coord.), discrete variable representation (DVR) types, number of grid points ($N$), and grid intervals used in GENIUSH to compute the vibrational states of the dimers. The final size of the direct product grid is $1.2 \times 10^8$ for $(H_2O)_2$, $1.2 \times 10^8$ for $CH_4{\cdot}H_2O$, and $8.8 \times 10^7$ for $(CH_4)_2$.

| Coord. | Min.[a] | Nuclear motion computations | | |
|---|---|---|---|---|
| | | DVR type[b] | $N$ | Grid interval |
| | | $(H_2O)_2$ | | |
| $R$ [Å] | 2.917 | PO Laguerre | 15 | scaled to [2.5,4.5] |
| $\theta$ [°] | 56.38 | Legendre | 31 | unscaled on (0,180) |
| $\phi$ [°] | 0.00 | Exponential | 25 | unscaled on [0,360) |
| $\alpha$ [°] | 180.00 | Exponential | 13 | unscaled on [0,360) |
| $\beta$ [°] | 60.40 | Legendre | 31 | unscaled on (0,180) |
| $\gamma$ [°] | 90.00 | Exponential | 25 | unscaled on [0,360) |
| | | $CH_4{\cdot}H_2O$ | | |
| $R$ [Å] | 3.457 | PO Laguerre | 15 | scaled to [2.5,6.0] |
| $\theta$ [°] | 116.14 | Legendre | 41 | unscaled on (0,180) |
| $\phi$ [°] | 90.00 | Exponential | 15 | unscaled on [0,360) |
| $\alpha$ [°] | 297.38 | Exponential | 9 | unscaled on [0,360) |
| $\beta$ [°] | 113.14 | Legendre | 61 | unscaled on (0,180) |
| $\gamma$ [°] | 292.85 | Exponential | 23 | unscaled on [0,360) |
| | | $(CH_4)_2$ | | |
| $R$ [Å] | 3.643 | PO Laguerre | 13 | scaled to [2.5,7.0] |
| $\theta$ [°] | 109.47 | Legendre | 51 | unscaled on (0,180) |
| $\phi$ [°] | 180.00 | Exponential | 17 | unscaled on [0,360) |
| $\alpha$ [°] | 120.00 | Exponential | 9 | unscaled on [0,360) |
| $\beta$ [°] | 109.47 | Legendre | 51 | unscaled on (0,180) |
| $\gamma$ [°] | 180.00 | Exponential | 17 | unscaled on [0,360) |

[a] Equilibrium geometry corresponding to the global minimum (GM) of the PESs at the $\langle r \rangle_0$ monomer structures.

[b] PO: potential optimization of the DVR points for a 1-dimensional model [103, 104].

extensive computations carried out during the present study. The main difference from earlier work [38, 39] is that this time we did not scale the Legendre DVR points used for the $\cos\theta$ and $\cos\beta$ coordinates, which together with an increased basis set size allowed us to converge the vibrational energies more tightly. For the $\phi, \alpha$, and $\gamma$ angles we use the same DVR parameters as in Refs. [38] and [39], but with an increased number of points. As a result of these changes, the final basis set and grid size for $CH_4{\cdot}H_2O$ is about one order of magnitude larger than in Refs. [38, 39].

### B. Vibrational states of the water dimer

The equilibrium structure of $(H_2O)_2$ has $C_s$ point-group symmetry. The collection of feasible exchanges between the possible permutation-inversion versions gives rise to the $G_{16}$ molecular symmetry group [105]. Reference [105] explains that vibrational states classified by the $C_s$ point-group symmetry form reducible representations in the $G_{16}$ molecular symmetry group and can be reduced to the direct sum of the following irreps of $G_{16}$:

$$\mathit{\Gamma}_{\mathrm{WW}}(\mathrm{A}') = \mathrm{A}_1^+ \oplus \mathrm{B}_1^+ \oplus \mathrm{E}^+ \oplus \mathrm{A}_2^- \oplus \mathrm{B}_2^- \oplus \mathrm{E}^- \tag{1}$$

$$\mathit{\Gamma}_{\mathrm{WW}}(\mathrm{A}'') = \mathrm{A}_2^+ \oplus \mathrm{B}_2^+ \oplus \mathrm{E}^+ \oplus \mathrm{A}_1^- \oplus \mathrm{B}_1^- \oplus \mathrm{E}^-. \tag{2}$$

Equations (1) and (2) correspond to the qualitative picture that the vibrational states split due to the interaction of the different permutation-inversion versions. According to Ref. [105], the $A_1^\pm$, $A_2^\pm$, $B_1^\pm$, $B_2^\pm$, and $E^\pm$ symmetry species have the following spin-statistical weights: 1, 3, 0, 6, and 3, respectively. Thus, states of $B_1^\pm$ symmetry do not exist, they are reported here for completeness.

Table XVI lists the vibrational energies obtained with the newly-developed WW19 PES (Section II) together with their $G_{16}$ symmetry label and qualitative assignment. The zero-point vibration (ZPV) manifold consists of 8 states and is spread over about 12 $\mathrm{cm}^{-1}$. The higher vibrational states are characterized by the prevailing type of nuclear motions, for example the second manifold can approximately be reduced to the donor torsion (DT), *i.e.,* librations of the donor water molecule around the hydrogen bond axis. Table XVII shows the comparison of the vibrational splittings derived from the newly-computed vibrational energies, earlier computations, and experiment. For the six vibrational splitting manifolds reported in the table, we observe a generally good agreement between the theoretical vibrational energies computed from recent water dimer PESs and experiment, with RMSE values ranging between 1.0 and 2.7 $\mathrm{cm}^{-1}$. The lowest RMSEs are given by the MB-pol and the current WW19 PES-PESs, with a negligible difference of 0.07 $\mathrm{cm}^{-1}$. These PESs are computed using essentially the same level of *ab initio* theory, but MB-pol is a flexible-monomer whereas WW19 PES is a rigid-monomer PES.

For a better understanding of the discrepancies between theory and experiment, measured by the RMSE values, one has to consider the various sources of possible errors in the theoretical treatment: the level of electron correlation treatment, the fitting error of a rigid-monomer vs. a full-dimensional surface, and the monomer flexibility effects in the quantum-nuclear-motion computations. In the following paragraphs, these aspects are analyzed in detail. Throughout the discussion, we focus on the six vibrational splitting manifolds for which results are collected in Table XVII.

Full-dimensional (12D), exact quantum-dynamical computations have been recently performed by Wang and Carrington [33] for $(H_2O)_2$, so intermolecular flexibility effects in the quantum dynamical computations can be rigorously assessed. The explicit inclusion of all 12

TABLE XVI. Vibrational energies and $G_{16}$ irrep labels of the $(H_2O)_2$ dimer obtained from the WW19 PES. The vibrational energies, in $\mathrm{cm}^{-1}$, are given with respect to the lowest-energy vibrational state.

| Index | $E$ [$\mathrm{cm}^{-1}$] | Irrep | Desc.[a] | Index | $E$ [$\mathrm{cm}^{-1}$] | Irrep | Desc.[a] |
|---|---|---|---|---|---|---|---|
| $D_\mathrm{e}$[b] | 1790.86 | | | | | | |
| $D_0$[b] | 1106.04 | | | | | | |
| ZPV[b] | 684.82 | | | | | | |
| 1[b] | 0 | $A_1^+$ | ZPV ($A'$) | 31–32 | 128.83 | $E^-$ | AT ($A''$) |
| 2–3 | 0.35 | $E^+$ | ZPV ($A'$) | 33 | 129.16 | $B_1^-$ | AT ($A''$) |
| 4 | 0.63 | $B_1^+$ | ZPV ($A'$) | 34–35 | 130.08 | $E^+$ | DTO ($A'$) |
| 5 | 11.42 | $A_2^-$ | ZPV ($A'$) | 36 | 133.25 | $B_1^+$ | DTO ($A'$) |
| 6–7 | 11.73 | $E^-$ | ZPV ($A'$) | 37 | 147.08 | $A_1^+$ | OO ($A'$) |
| 8 | 11.98 | $B_2^-$ | ZPV ($A'$) | 38–39 | 147.97 | $E^+$ | OO ($A'$) |
| 9 | 60.22 | $A_2^+$ | DT ($A''$) | 40 | 148.68 | $B_1^+$ | OO ($A'$) |
| 10–11 | 61.15 | $E^+$ | DT ($A''$) | 41 | 152.11 | $A_2^-$ | OO ($A'$) |
| 12 | 62.12 | $B_2^+$ | DT ($A''$) | 42–43 | 153.05 | $E^-$ | OO ($A'$) |
| 13 | 105.81 | $A_1^+$ | AW ($A''$) | 44 | 153.81 | $B_2^-$ | OO ($A'$) |
| 14–15 | 106.77 | $E^+$ | AW ($A''$) | 45 | 172.05 | $A_1^+$ | |
| 16 | 108.03 | $B_1^+$ | AW ($A''$) | 46–47 | 173.01 | $E^+$ | |
| 17–18 | 108.33 | $E^-$ | AW ($A''$) | 48–49 | 173.94 | $E^-$ | DTO ($A'$)[c] |
| 19 | 108.49 | $A_2^-$ | AW ($A''$) | 50 | 174.68 | $A_2^+$ | |
| 20 | 108.62 | $B_2^-$ | AW ($A''$) | 51 | 175.56 | $A_1^-$ | |
| 21 | 109.48 | $A_1^-$ | DT ($A''$) | 52 | 176.25 | $B_1^-$ | |
| 22–23 | 112.10 | $E^-$ | DT ($A''$) | 53 | 176.72 | $A_2^-$ | DTO ($A'$) |
| 24 | 114.07 | $B_1^-$ | DT ($A''$) | 54–55 | 186.86 | $E^-$ | DTO ($A'$)[c] |
| 25 | 114.28 | $A_2^+$ | AT ($A''$) | 56 | 187.80 | $B_1^+$ | |
| 26–27 | 117.50 | $E^+$ | AT ($A''$) | 57 | 189.05 | $B_2^+$ | |
| 28 | 122.58 | $B_2^+$ | AT ($A''$) | 58–59 | 189.08 | $E^+$ | |
| 29 | 124.40 | $A_1^+$ | DTO ($A'$) | 60 | 193.13 | $B_2^-$ | DTO ($A'$) |
| 30 | 128.69 | $A_1^-$ | AT ($A''$) | | | | |

[a] ZPV: zero-point vibration, DT: donor torsion, AW: acceptor wag, AT: acceptor twist, DTO: donor-torsion overtone, OO: intermonomer stretching vibration. The $A'$ and $A''$ $C_\mathrm{s}$ irrep labels are used to denote the symmetry of a vibrational state, which split up according to Eqs. (1) and (2).

[b] $D_\mathrm{e}$: energy of the dissociation asymptote measured from the minimum value of the 6-dimensional PES corresponding to the $\langle r\rangle_0$ rigid-monomer structure; $D_0$: smallest vibrational energy value measured from the dissociation asymptote; ZPV: zero-point vibrational energy ($A_1^+$ species) measured from the bottom of the 6D PES. Note that $E[\mathrm{ZPV}, A_1^+] = D_\mathrm{e} - D_0$.

[c] Further analysis is necessary to decide which $E^-$ state belongs to the donor-torsion overtone (DTO) splitting manifold.

vibrational degrees of freedom results in an RMSE smaller by 0.07 $\mathrm{cm}^{-1}$ than the earlier 6D+6D computations of Leforestier *et al.* [13], which included monomer flexibility effects in an adiabatic fashion. This comparison, already made in Ref. [33], shows that the {6D+6D} approximation works very well for intermonomer rovibrational modes. Furthermore, the exact, 12-dimensional quantum dynamical computations also confirm that the remaining discrepancies between the-

TABLE XVII. Vibrational splittings for the $(H_2O)_2$ dimer: experimental vs. theoretical results corresponding to different PESs with rigid, {6D}, adiabatic flexible, {6D + 6D}, and fully coupled, flexible monomers, {12D}.

| Label[a] | | Expt.[b] | This work[c] {6D} | CCpol-8sf[d] {6D + 6D} | CCpol-8sf[e] {12D} | CCpol-8s[f] {6D} | CCpol-5s[g] {6D} | MB-pol[h] {6D + 6D} | HBB1[i] {6D} | HBB2[j] {6D + 6D} |
|---|---|---|---|---|---|---|---|---|---|---|
| ZPV ($A'$) | $o_1$ | 0 | 0 | 0 | 0 | 0 | 0 | 0 | 0 | 0 |
| | $i_1$ | 0.75 | 0.63 | 0.72 | 0.69 | 0.79 | 0.69 | 0.81 | 0.75 | 0.68 |
| | $o_2$ | 11.18 | 11.70 | 12.75 | 12.58 | 12.31 | 13.28 | 12.05 | 13.33 | 10.16 |
| | $i_2$ | 0.65 | 0.56 | 0.61 | 0.58 | 0.67 | 0.66 | 0.69 | 0.64 | 0.60 |
| DT ($A''$) | $o_1$ | | 111.78 | 113.35 | 113.34 | 113.19 | 118.71 | 113.83 | 116.10 | 116.54 |
| | $i_1$ | | 4.59 | 5.91 | 5.67 | 6.46 | 4.59 | 5.61 | 6.36 | 4.83 |
| | $o_2$ | 64.52 | 61.17 | 61.33 | 61.92 | 61.58 | 60.48 | 61.31 | 60.77 | 67.18 |
| | $i_2$ | 2.54 | 1.90 | 2.48 | 2.38 | 2.76 | 1.50 | 2.54 | 2.38 | 2.03 |
| AW ($A'$) | $o_1$ | 107.93 | 106.92 | 109.23 | 109.34 | 109.37 | 110.94 | 108.38 | 107.00 | 105.35 |
| | $i_1$ | 2.95 | 2.22 | 3.29 | 3.04 | 3.89 | 3.06 | 3.24 | 3.92 | 1.99 |
| | $o_2$ | 108.89 | 108.55 | 107.82 | 108.11 | 109.57 | 115.66 | 108.87 | 106.13 | 105.78 |
| | $i_2$ | 0.02 | 0.12 | 0.10 | 0.06 | 0.03 | 0.50 | 0.13 | 0.01 | 0.03 |
| AT ($A''$) | $o_1$ | | 128.93 | 132.10 | 132.22 | 132.11 | 129.39 | 129.44 | 130.34 | 128.91 |
| | $i_1$ | | 0.47 | 1.48 | 1.29 | 1.02 | 2.80 | 0.24 | 1.12 | 0.74 |
| | $o_2$ | 120.19 | 119.34 | 117.50 | 117.61 | 117.86 | 117.76 | 119.07 | 116.34 | 121.01 |
| | $i_2$ | 9.39 | 8.30 | 8.67 | 8.34 | 9.83 | 9.89 | 10.15 | 9.67 | 8.41 |
| DTO ($A'$) | $o_1$ | | 128.83 | 128.22 | 128.51 | 128.12 | 150.13 | | 140.16 | |
| | $i_1$ | | 8.85 | 9.19 | 8.94 | 10.90 | 2.42 | | 2.72 | |
| | $o_2$ | | 184.93 | 184.57 | 185.01 | 185.38 | 189.58 | | 183.84 | |
| | $i_2$ | | 16.41 | 18.3 | 18.2 | 19.60 | 18.34 | | 19.17 | |
| OO ($A'$) | $o_1$ | | 147.88 | 143.20 | 143.15 | 147.61 | 133.15 | 149.44 | 127.09 | 145.00 |
| | $i_1$ | | 1.60 | 3.27 | 3.11 | 2.50 | 8.47 | 1.97 | 8.93 | 3.48 |
| | $o_2$ | 153.62 | 152.96 | 149.63 | 149.49 | 153.32 | 156.92 | 154.31 | 147.79 | 148.57 |
| | $i_2$ | 1.88 | 1.70 | 1.23 | 1.13 | 1.98 | 1.75 | 2.41 | 1.28 | 1.14 |
| Average error | | | −0.65 | −0.70 | −0.71 | −0.04 | 0.66 | −0.04 | −1.12 | −0.89 |
| RMSE | | | 1.11 | 1.75 | 1.68 | 1.21 | 2.69 | 1.04 | 2.44 | 2.03 |

[a] ZPV: zero-point vibration, DT: donor torsion, AW: acceptor wag, AT: acceptor twist, DTO: donor-torsion overtone, OO: intermonomer stretching vibration. The $A'$ and $A''$ $C_\mathrm{s}$ irrep labels are used to denote the symmetry of a vibrational state, which split up according to Eqs. (1) and (2).

[b] Data taken from Table 4 of Ref. [14], which summarizes and compares available experimental and computational results. The original experimental results are available in Refs. [31, 32, 106–108].

[c] The spacing of the one-dimensional irreps within a splitting is calculated from the vibrational energies given in Table XVI using the relations [9]: $o_n = [E(\mathrm{A}_n^{\pm}) + E(\mathrm{B}_n^{\pm})]/2$ and $i_n = E(\mathrm{B}_n^{\pm}) - E(\mathrm{A}_n^{\pm})$ (with $n = 1, 2$), except for $o_1$ of the ZPV, which is 0 by definition.

[d] Rovibrational computations of Ref. [13] (Fig. 3).

[e] Rovibrational computations of Ref. [33] rigorously including all (12) vibrational degrees of freedom.

[f] Results of Ref. [9], recomputed in Ref. [13] (Fig. 2). Notice that earlier assignments of the DTO and OO manifolds (for both theory and experiment) were changed in Ref. [13]. The new assignments agree with ours and we used them for all literature data.

[g] Table I of Ref. [8] with reassignment as in footnote f.

[h] Table 4 of Ref. [14].

[i] Table IV of Ref. [10] with reassignment as in footnote f.

[j] The values originally computed in Ref. [34] and then quoted in Table 4 of Ref. [14] are slightly different, we took the latter ones.

ory and experiment must be due to inaccuracies and uncertainties in the PES representation discussed in Sec. II D.

The comparison of the results from 6D and 12D PESs confirms an earlier opinion expressed in Refs. [5] and [13] that the inclusion of monomer flexibility effects does not lead to any significant improvement of the theoretical results in the present energy range studied at the present level of accuracy. This may seem counterintuitive since monomer-flexibility effects for individual levels are generally on the order of 1 $\mathrm{cm}^{-1}$ as it can be seen by comparison of the columns CCpol-8sf {12D} and CCpol-8s {6D}. Since CCpol-8s is CCpol-8sf computed at the $\langle r \rangle_0$ geometry of monomers, these differences are due only to monomer flexibility effects. However, the overall RMSE value for CCpol-8s {6D} is actually lower than that for CCpol-8sf {12D} (or CCpol-8sf {6D+6D}). Also, the RMSE for CCpol-8s {6D} is only slightly worse, by 0.17 $\mathrm{cm}^{-1}$, than for MB-pol {6D+6D}. The explanation for this unexpected behaviour is that it is much more difficult to fit a 12D PES than a 6D PES, both in terms of adequate covering of the space by grid points and in terms of the more complicated form of the fitting function. Thus, the former PESs may have larger numerical uncertainties than the latter ones, which is then reflected in the spectral results.

According to Table XVII, the WW19 PES performs remarkably well. This observation indicates that the general automated PES development procedures, used in the present work, outperform the earlier manual PES-development methodologies (in which often application-specific strategies were used by adding grid points along the most important tunneling paths, etc.). It is interesting to further study the performance of the WW19 PES in comparison with the CCpol-5s and the CCpol-8s PESs (Table XVII). CCpol-5s and CCpol-8s were fitted to the same set of interaction energies, but the latter PES used a more elaborate fitting function (the fit RMSEs of the two PESs for negative $E_{\mathrm{int}}$ interaction energies were 31 and 3.5 $\mathrm{cm}^{-1}$, respectively). The more accurate fit led to a significant decrease of RMSE with respect to the experimental spectra, by 1.48 $\mathrm{cm}^{-1}$. To construct the WW19 PES, the same functional form was used as for CCpol-8s, but these two surfaces were fitted to interaction energies obtained at different *ab initio* levels of theory. On one hand, the data points for the WW19 PES are more accurate since the CCSD(T)−MP2 correction term was computed using the CBS extrapolations from aug-cc-pVTZ and aug-cc-pVQZ plus midbond bases (see Sec. II), whereas it was obtained only using the aug-cc-pVTZ plus midbond basis (no extrapolations) for the CCpol-5s/8s PESs. On the other hand, all electrons were correlated in computing the CCpol PESs. Apparently, the former effect is slightly more important than the latter, since the RMSE with respect to experiment is lower for the WW19 PES by 0.10 $\mathrm{cm}^{-1}$. Finally, we mention the monomer-geometry effect, which affects the rigid-monomer approximation (for further details see also Section V about dissociation energies). Both PESs used vibrationally averaged monomer structures, but in WW19 PES this structure is $\langle r \rangle_0$ coming from a highly accurate CVRQD water monomer

PES [83, 84, 109], whereas CCpol-8s used the GED $\langle r^{-1}\rangle_0^{-1}$ structure from Ref. [87]. It would be possible to check this effect, but it is likely to be small, so we have not performed this test.

### C. Vibrational states of the methane-water dimer

The methane-water dimer has two equilibrium structures, both of $C_\mathrm{s}$ point-group symmetry. In the global minimum (GM), the water molecule is the proton donor, while in the secondary minimum (SM) the donor-acceptor roles are exchanged (see Section II).

The molecular symmetry group of $CH_4{\cdot}H_2O$ is $G_{48}$ (for the $G_{48}$ character table and further details see Refs. [38, 39]). The spin-statistical weights for the different symmetry species were given in the Supplementary Information of Ref. [38]. Due to the interaction of the various permutation-inversion versions, the totally symmetric ($A'$) vibrational states (with respect to the symmetry plane of the GM or SM minima) split up and form a representation in the $G_{48}$ group which is the direct sum of the following irreps [38]:

$$\mathit{\Gamma}_\mathrm{MW}(\mathrm{A}') = \mathrm{A}_1^+ \oplus \mathrm{E}^+ \oplus \mathrm{F}_1^+ \oplus 2\mathrm{F}_2^+ \oplus \mathrm{A}_2^- \oplus \mathrm{E}^- \oplus 2\mathrm{F}_1^- \oplus \mathrm{F}_2^- \tag{3}$$

For example, the (totally symmetric) ZPV state (in either the global or the secondary minimum well) splits up according to $\mathit{\Gamma}_\mathrm{MW}(\mathrm{A}')$ given in Eq. (3). Since the symmetry properties of the two minima are identical, we can make a (non-rigorous) qualitative assignment of vibrational states to the GM or the SM well by identifying structural differences (different expectation values of geometrical parameters) and by analyzing characteristics of wave-function plots.

Table XVIII presents the computed vibrational states corresponding to the newly-developed WM19 PES. In the energy range included in the table, all computed states are given. Most of these states belong to the ZPV manifold. The highest state included is the (lowest-energy) fundamental intermolecular stretching vibration (tentatively assigned to belong to the global minimum). Similarly to the zero-point vibrational manifold, this $A'$-symmetry fundamental stretching mode also splits up according to Eq. (3) (in Table XVIII, only the lowest-energy $\mathrm{A}_1^+$ level is given).

In addition to the newly computed vibrational states, we cite the results of earlier computations [38, 39] using the first quantitatively correct intermolecular PES [16], which used the $\langle r^{-1}\rangle_0^{-1}$ GED monomer structures, and a more recent, full-dimensional PES [17], which allowed us to use the $\langle r\rangle_0$ monomer structures in the (ro)vibrational computations.

The high-resolution experimental transitions available in the literature [36] were assigned to the ZPV rovibrational splitting manifold of the global minimum [38], based on rovibrational computations (up to $J = 2$ rotational quantum number) and the PES of Ref. [16]. A detailed comparison between the experimental and the computed transition energies was given in Ref. [38]. Note that it was necessary to reassign the $\mathrm{F}_1^+$ and $\mathrm{F}_2^+$ irrep labels in Ref. [39] (Table XVIII applies the new assignments) using the automated coupled-rotor decomposition (CRD) scheme of Ref. [39].

Three of us have carried out similar computations (up to $J = 2$) [39] using the QCHB15 PES and $\langle r \rangle_0$ monomer structures and obtained a similarly good agreement with the experimental transitions [36] as in the earlier computations [38] with the AOSz05 PES [16]. A similar direct comparison using the WM19 PES with the experimental (rotational) transition energies will be reported later [101]. We would like to point out, however, that the available experimental dataset [36] includes only rotational excitations within a vibrational band, so the vibrational spacings predicted by the different PESs (of different quality) cannot be assessed based on that experiment.

While detailed comparison of vibrational levels with experiment is not yet possible, we can compare the vibrational states obtained with the three PESs. The results and comparison with the present work is included in Table XVIII, in which we collect all vibrational states up to the lowest energy species of the stretching fundamental (note that for the different PESs there is a different number of states up to this level). A general discussion of the dissociation energies is postponed to Section V, now we focus on the vibrational energies.

The RMSD of the vibrational energies of the QCHB15 and AOSz05 levels relative to the WM19 PES levels are calculated for the values listed in Table XVIII, *i.e.,* in each case energies are measured from the ground state of a given method. The RMSD would have been much larger if the vibrational levels were measured from the dissociation limit. RMSDs of the QCHB15($\langle r \rangle_0$) and AOSz05($\langle r_{\mathrm{GED}} \rangle$) levels with respect to the WM19($\langle r \rangle_0$) PES levels are 0.78, and 1.54 $\mathrm{cm}^{-1}$, respectively. In the ZPV(GM) splitting manifold, the $\mathrm{F}_2^+$ species of the upper part of the splitting appears to be an outlier with discrepancies as large as 1.13 and 2.31 $\mathrm{cm}^{-1}$ for QCHB15 and AOSz05, respectively. All other levels of the ZPV(GM) manifold as well as the lowest-energy, $\mathrm{A}_1^+$ species of Stre(GM) are in reasonable agreement in the three different computations. For the zero-point vibration ($\mathrm{A}_1^+$ species) corresponding to the secondary minimum, labelled with ZPV(SM), we observe larger deviations, 2.29 and 4.00 $\mathrm{cm}^{-1}$, for the QCHB15 and AOSZ05, respectively.

While the discrepancies in relative quantities are reasonably small, the discrepancies in absolute quantities such as ZPV energies are fairly large, in the case of AOSz05 it is about 12 $\mathrm{cm}^{-1}$. Perhaps surprisingly, the $D_0$ of AOSz05 is only 1 $\mathrm{cm}^{-1}$ off, but this is simply due to the fact that its $D_{\mathrm{e}}$ is 11 $\mathrm{cm}^{-1}$ too small and the errors cancel.

In general, QCHB15 results are closer to WM19 PES than the AOSz05 ones. This can be expected since the basis set used in Ref. [16] was of augmented triple-zeta quality and no CBS extrapolations have been performed, *i.e.,* the errors due to basis set truncation are larger than in the QCHB15 or WM19 PESs. In addition, the $r_{\mathrm{GED}}$ monomer geometry was used in the former case, while the $\langle r \rangle_0$ one, believed to lead to better results, was used in the latter two cases.

TABLE XVIII. Comparison of vibrational energies of $CH_4{\cdot}H_2O$, in $cm^{-1}$, obtained with three different potential energy surfaces. The vibrational energies are given with respect to the lowest-energy state in each column. The deviations of the literature vibrational energies from the WM19 PES results are given in parentheses.

| Label | WM19 PES $\langle r\rangle_0$[e] | QCHB15 PES[a] $\langle r\rangle_0$[e] | AOSz05 PES[b] $r_\mathrm{GED}$[e] | Irrep[c] | Desc.[d] |
|---|---|---|---|---|---|
| $D_\mathrm{e}$[f] | 367.82 | 371.68 | 356.68 | | |
| $D_0$[f] | 148.87 | 152.03 | 149.89 | | |
| ZPV(GM)[f] | 218.95 | 219.65 | 206.79 | | |
| 1 | 0 | 0 | 0 | $A_1^+$ | ZPV(GM) |
| 2–4 | 4.28 | 4.18 (0.10) | 4.76 (−0.48) | $F_2^+$ | ZPV(GM) |
| 5 | 6.77 | 6.65 (0.13) | 6.93 (−0.16) | $A_2^-$ | ZPV(GM) |
| 6–8 | 10.58 | 10.33 (0.25) | 11.19 (−0.61) | $F_1^-$ | ZPV(GM) |
| 9–11 | 31.25 | 31.59 (−0.34) | 32.71 (−1.36) | $F_2^-$ | ZPV(GM) |
| 12–14 | 31.25 | 30.12 (1.13) | 28.94 (2.31) | $F_2^+$ | ZPV(GM) |
| 15–17 | 31.70 | 31.69 (0.01) | 32.61 (−1.01) | $F_1^-$ | ZPV(GM) |
| 18–19 | 35.24 | 35.14 (0.10) | 36.36 (−1.12) | $E^-$ | ZPV(GM) |
| 20–22 | 35.72 | 35.54 (0.17) | 36.32 (−0.61) | $F_1^+$ | ZPV(GM) |
| 23–24 | 35.81 | 35.72 (0.10) | 35.74 (0.07) | $E^+$ | ZPV(GM) |
| 25 | 38.40 | 36.11 (2.29) | 34.41 (4.00) | $A_1^+$ | ZPV(SM) |
| 26–28 | 42.05 | 41.17 (0.89) | 41.13 (0.93) | $F_2^+$ | * |
| 29–30 | 46.69 | 47.10 (−0.41) | 47.97 (−1.28) | $E^+$ | * |
| | | 47.17 | 45.83 | $F_1^-$ | * |
| | | | 47.16 | $E^-$ | * |
| 31 | 47.36 | 47.66 (−0.29) | 48.67 (−1.31) | $A_1^+$ | Stre(GM) |
| RMSD[g] | | 0.78 | 1.5 | | |

[a] Vibrational states computed in Ref. [39] using the PES of Ref. [17]. The $D_\mathrm{e}$ value was computed in Ref. Ref. [39], whereas Table X quotes the value from the orginal paper.

[b] Vibrational states computed in Ref. [38] using the PES of Ref. [16]. The $D_\mathrm{e}$ value was computed in Ref. Ref. [38], whereas Table X quotes the value from the orginal paper.

[c] Irrep label of the $G_{48}$ molecular symmetry group of $CH_4{\cdot}H_2O$.

[d] Qualitative assignment of the vibrational state. ZPV(GM): 24-fold splitting manifold of the zero-point vibrational state corresponding to the global minimum, see also Eq. (3); ZPV(SM): splitting manfold of the zero-point vibrational state corresponding to the secondary minimum (only the lowest-energy level is shown); Stre(GM): splitting manifold of the zero-point vibrational state corresponding to the secondary minimum (only the lowest-energy level is shown); *: vibrational states left without assignment.

[e] Rigid-monomer structures used are defined in Table II.

[f] See footnote b to Table XVI.

[g] Root-mean-squared deviation of the vibrational energies relative to the ground-state energy from a given method. The reference are the WM19 PES results.

However, the effects coming from such differences in monomer geometries are expected to be smaller than the discrepancies discussed above.

The QCHB15 and WM19 PESs give reasonably close results and it will be interesting to confront them with experiment. At this point, we believe that the WM19 PES results are more accurate. As discussed earlier, Qu *et al.* [17] used the CCSD(T)-F12b method which includes explicit electron correlation terms and gives more accurate energies than the regular orbital CCSD(T), but they used a much smaller basis set than we used and they performed no CBS extrapolation. Even more severe approximation is the neglect of the CP correction, amounting in their basis to 26 $\mathrm{cm}^{-1}$ [17]. Thus, their interaction energies include spurious basis set superposition effects. Furthermore, an 18D fit is considerably more difficult than a 6D one and a 6D cut of the 18D surface is expected to have larger errors than a direct 6D fit. In particular, we expect that the calculations based on the WM19 PES ($\langle r \rangle_0$) should provide the most accurate theoretical ZPV(GM)–ZPV(SM) separation energy. It would be important to know this value accurately, as it corresponds to the exchange of the donor-acceptor roles between the methane and water molecules.

In order to resolve the observed discrepancy between the three PESs for the energy separation of the two $\mathrm{F}_2^+$ levels within the ZPV(GM) and for the ZPV(GM)–ZPV(SM) difference, further theoretical and experimental work is necessary. It is interesting to note that the rovibrational transitions between the two $\mathrm{F}_2^+$ ZPV(GM) levels should have been seen within the 18–35.5 $\mathrm{cm}^{-1}$ range of the high-resolution experiments of Ref. [36] (the symmetric-top selection rules had been derived in the Supplementary Information of Ref. [38]). The ZPV(SM)–ZPV(GM) separation might also be found in the same experimental data set, although this cannot be stated with certainty due to the relatively large uncertainty of the theoretical predictions, with the mean value being just at the upper limit of the experimental energy range. In short, further experimental work or at least a more detailed analysis of the unpublished part of the data set of Ref. [36] would help to proceed with the validation of the available PESs. *Vice versa*, the computed (ro)vibrational energies (now available using three different potential energy surfaces) could facilitate the analysis and assignment of the experimentally observed rovibrational transitions through a line-by-line comparison.

### D. Vibrational states of the methane dimer

The global minimum of the methane dimer has $D_{3\mathrm{d}}$ point-group symmetry (see Sec. II). The molecular symmetry group of the dimer is $G_{576}$ [110, 111], for which the character table was generated using the GAP program package [112] according to the instructions of Ref. [111] (the $G_{576}$ character table is reproduced in SI). Reference [111] also gives the spin-statistical weights of $(\mathrm{CH}_4)_2$, and all spatial functions can be matched with at least one spin functions to satisfy the spin-statistics theorem [113].

The vibrational states of $D_{3\mathrm{d}}$ point-group symmetry are split due to the feasible exchange of the permutation-inversion versions of the complex. For a vibration transforming according to the totally symmetric irrep of the $D_{3\mathrm{d}}$ point group, such as the zero-point vibration, the splitting includes the following species of the $G_{576}$ group (in the present work, we use the irrep labels and class ordering according to the GAP-generated table):

$$\mathit{\Gamma}_{\mathrm{MM}}(\mathrm{A}_{1\mathrm{g}}) = \mathrm{X}_1(1) \oplus \mathrm{X}_8(2) \oplus \mathrm{X}_{11}(6) \oplus \mathrm{X}_{13}(9) \oplus 2\mathrm{X}_{15}(9) \oplus \mathrm{X}_{16}(12) \tag{4}$$

Table XIX shows the computed vibrational states. As in the $CH_4{\cdot}H_2O$ case, we included all the states up to the lowest-energy level of the fundamental stretching vibration (identified by its symmetry label and by finding a node along the intermolecular distance coordinate ($R$) in the wave function). This state is number 57 in our computations. Among the remaining 56 listed states, most (48 states) could be assigned to the ZPV splitting manifold.

To the best of our knowledge, the present work reports the first spectroscopic quality vibrational calculations for the methane dimer. We are not aware of any high-resolution experimental measurements of the bound states of $(CH_4)_2$. Further details on the $(CH_4)_2$ symmetry analysis, including higher-energy vibrational as well as rovibrational states will be provided in a forthcoming publication [101].

## V. REDUCED-DIMENSIONALITY MODELS IN COMPUTATION OF DISSOCIATION ENERGIES

In addition to the comparison of experimental and theoretical (ro)vibrational energies, the dissociation energy, $D_0$, is also an important measure for the quality of a PES. While the low-energy spectral transitions are differential quantities, and thus useful to test the curvature of the PES, the dissociation energy measures an interplay of the absolute depth of the PES well and its curvature near the minimum structure.

Unfortunately, $D_0$ is much more difficult to measure than spectra, but recently an accurate measurement was performed for the water dimer [55] with an uncertainty of only 10 $\mathrm{cm}^{-1}$. Table XX collects dissociation energies (as well as zero-point-vibration energies) of the water dimer from various PESs and various quantum nuclear motion computation methods. For the MB-pol PES [14], we could not find any calculations of $D_0$ in the literature, so it is not included in the table.

For the $CH_4{\cdot}H_2O$ and $(CH_4)_2$ dimers, we are not aware of any experimental $D_0$ values. Table XVIII has already compared the dissociation energies obtained with three different PESs for $CH_4{\cdot}H_2O$, whereas Table XIX has reported our value for $(CH_4)_2$. Note that this is apparently the first value of $D_0$ ever reported for the methane dimer. In the following paragraphs we will first discuss only the water dimer. Near the end of this sections, we will discuss Table XXI which

TABLE XIX. Energies and $G_{576}$ irrep labels of the vibrational states of $(CH_4)_2$ computed with MM19 PES. The vibrational energies are given with respect to the lowest-energy state.

| Index | $E$ [cm$^{-1}$][a] | Irrep label[b] | Desc.[c] |
|---|---|---|---|
| $D_e$[d] | 190.23 | | |
| $D_0$[d] | 103.61 | | |
| ZPV[d] | 86.62 | | |
| 1[d] | 0 | $X_1(1)$ | ZPV($A_{1g}$) |
| 2–7 | 8.99 | $X_{11}(6)$ | ZPV($A_{1g}$) |
| 8–16 | 18.03 | $X_{15}(9)$ | ZPV($A_{1g}$) |
| 17–25 | 19.31 | $X_{13}(9)$ | ZPV($A_{1g}$) |
| 26–34 | 19.36 | $X_{15}(9)$ | ZPV($A_{1g}$) |
| 35–40 | 31.43 (0.01) | $X_{11}(6)$ | |
| 41–44 | 31.71 | $X_9(2)$ | |
| 45–56 | 32.17 (0.01) | $X_{16}(12)$ | ZPV($A_{1g}$) |
| 57 | 32.93 | $X_1(1)$ | Stre($A_{1g}$) |

[a] The energy splitting of degenerate states due to an incomplete convergence is given in parentheses when it is larger than or equal to 0.01 cm$^{-1}$.

[b] Irrep label of the $G_{576}$ group. The multiplicity of the irrep is given in parentheses.

[c] Qualitative description of the vibration and its point-group symmetry. The $G_{576}$ symmetry species in the splitting of a totally symmetric vibration in the $D_{3d}$ point group are listed in Eq. (4).

[d] See footnote b to Table XVI with the difference that the lowest-energy state has now the $X_1(1)$ irrep label instead of $A_1^+$.

collects our results for all three dimers. The general observations made in this section should be transferable to other molecular dimers.

The interplay of theory and experiment in investigations of the water dimer dissociation energy has an at least a 40-year-old history. Since 1979, the experimental value of $D_0 = 1256 \pm 175$ cm$^{-1}$ [114] (more precisely, the experimental enthalpy of association) was considered to be the benchmark value for theory. Thus, when the first $D_0 = 1067$ cm$^{-1}$ value based on a fully first-principles approach was published [3, 115] in 2000, it was considered as a poor performance of theory since it was slightly beyond experimental uncertainties. The next *ab initio* value, 1042 cm$^{-1}$ (Ref. [10]) published in 2006, was even further from experiment. The deviation from the experimental result got only slightly smaller but within experimental uncertainties in 2008 and 2009, when values around 1100 cm$^{-1}$ were obtained from several computations [8, 9, 12]. Note that no uncertainties were attached to the theoretical results. Eventually, the correctness of theoretical results was confirmed by a new, much more accurate experimental value, $D_0 = 1105 \pm 10$ cm$^{-1}$, published in 2011 [55].

Table XX presents the $D_0$ values obtained with the WW19 PES as well as with earlier PESs available in the literature. In two cases, we have repeated literature calculations. For the HBB1

PES, we found a 5 cm$^{-1}$ deviation in $D_0$ and an 8 cm$^{-1}$ deviations in $D_\mathrm{e}$ from the published values [10], probably due to slightly different monomer geometries. Calculations of Ref. [10] presumably used in their 6D calculations the O–H bond length of 0.9615 Å and the H–O–H angle of 104.2 degrees, the equilibrium isolated monomer geometry at the level of theory applied in that work (see page 2 of Ref. [10]). This geometry is labelled in Table XX as $r^*_\mathrm{eq}$. We used the $r_\mathrm{eq}$ set of values from Table II which has the bond shorter by 0.004 Å and the angle larger by 0.3 degrees. We performed calculations with the same $r_\mathrm{eq}$ also using the HBB2 PES (there are no 6D published results for this surface).

Table XX includes also the depths of PESs, $D_\mathrm{e} = -U_\mathrm{min}$ (for all flexible-monomer PESs) or $D_\mathrm{e} = -V_\mathrm{min}$ (for all rigid-monomer PESs), some of them already displayed in Tables VII and IX. The BO benchmark values of Lane [57] are matched to all digits by the 12D CCpol-8sf [13] and CCpol-8sfIR [15, 33] PESs (note that CCpol-8sfIR is a minor modification of CCpol-8sf). This agreement is partly due to cancellations of errors since the uncertainties of *ab initio* data used to fit these PESs are similar to those of WW19 PES, *i.e.*, are about 30 cm$^{-1}$. The depths of the HBB1 and HBB2 PESs are different by 89 and 15 cm$^{-1}$ from the BO benchmark, respectively, while that of the MB-pol PES (not listed in Table XX) is 40 cm$^{-1}$. Thus, all recent 12D PES give similarly accurate $D_\mathrm{e}$. In the case of 6D PES, comparisons with the BO benchmark is appropriate only for the surfaces with $r_\mathrm{eq}$ monomers since the monomers are close to their equilibrium configuration in the minima of 12D PESs. Indeed, the $D_\mathrm{e}$ of HBB2($r_\mathrm{eq}$) is only 32 cm$^{-1}$ from the benchmark. For PESs with monomers at $\langle r\rangle_0$, such comparisons are not appropriate since the limit $D_\mathrm{e}$ in this case is significantly larger than the 12D limit. Table XX shows that the included PESs($\langle r\rangle_0$) have $D_\mathrm{e}$'s in a narrow range 1778–1791 cm$^{-1}$ (except for HBB1). The uncertainty of the energy points used for the WM19 PES was estimated in Sec. II (cf. Table VII) to be 30 cm$^{-1}$ with respect to the BO limiting value. The uncertainties due to the fitting errors and to the monomer geometry extrapolations are about 6 and 5 cm$^{-1}$, respectively, in the region of the potential well.

More information can be obtained by looking at the values of $D_0$'s which we can compare to the experimental result. Table XX shows that $D_0$'s are, as expected, well correlated with $D_\mathrm{e}$'s. The change of the monomer geometry from $r_\mathrm{eq}$ to $\langle r\rangle_0$ increases $D_0$ quite dramatically, by 41 cm$^{-1}$ in the case of the HBB1 surface, and it becomes very close to the 12-dimensional diffusion Monte Carlo (DMC) result, differing from it only by 8 cm$^{-1}$. This is yet another example showing the importance of using the $\langle r\rangle_0$ monomer geometries in reduced-dimensionality computations. The full-dimensional DMC value for the HBB1 PES is 63 cm$^{-1}$ smaller than the experimental result [55].

Similar observations can be made for the $D_0$ values obtained with the HBB2 PES. In particular, the $r_\mathrm{eq}$ to $\langle r\rangle_0$ and the 6D to 12D improvements introduce 43 cm$^{-1}$ and 10 ± 4 cm$^{-1}$ corrections, respectively. Thus, HBB2 provides an excellent demonstration of the importance of using the proper monomer geometry: with $r_\mathrm{eq}$, HHB2 gives $D_0$ that is 55 cm$^{-1}$ from experiment, whereas with $\langle r \rangle_0$, only 12 $\mathrm{cm}^{-1}$. There is a fairly significant difference, $7 \pm 4$ $\mathrm{cm}^{-1}$, in the value of $D_0$ between the 6D+6D calculations of Ref. [34] and the 12-dimensional DMC calculations of Ref. [12]. It was initially assumed that the large deviation is due to the adiabatic approximation in the 6D+6D treatment. However, the recent fully 12D calculations of Wang and Carrington [33] (see further discussion below) show that this approximation introduces only a 2 $\mathrm{cm}^{-1}$ error in $D_0$. Thus, the true 12D $D_0$ for HBB2 is about 1098 $\mathrm{cm}^{-1}$, showing that the agreement of DMC to within 2 $\mathrm{cm}^{-1}$ with the experimental value is incidental. Although the value of 1098 $\mathrm{cm}^{-1}$ is outside the uncertainty range of the DMC result, this is not unexpected. One should realize that the uncertainties given by the DMC method are only statistical, i.e., do not include systematic deviations since these are unknown.

The computations with the CCpol-8sf PES and its 6D equivalent, CCpol-8s, show a 16 $\mathrm{cm}^{-1}$ increase of $D_0$ when moving from the rigid-monomer at a vibrationally averaged geometry, here the $r_{\mathrm{GED}} = \langle r^{-1} \rangle_0^{-1}$ geometry, to the full-dimensional vibrational computations. This shift is larger than for HBB2 (5 $\mathrm{cm}^{-1}$ if we use the estimated 12D value of $D_0 = 1098$ $\mathrm{cm}^{-1}$). This may indicate that the $\langle r \rangle_0$ geometry gives a better approximation of flexible-monomer results than the $r_{\mathrm{GED}}$ geometry.

Until recently, the only way to include monomer-flexibility effects in computations of the water dimer dimer spectra was to use the 6D+6D adiabatic approximation method of Leforestier *et al.* [5, 116]. The only exception was the ground state energy, which could be computed using DMC, but uncertainties of such calculations are quite large. A recent breakthrough was the development of a fully 12D method by Wang and Carrington [33]. Application of this method to the water dimer demonstrated that the 6D+6D approach is quite accurate, see the transition energies listed in Table XVII, with only a fraction of $\mathrm{cm}^{-1}$ discrepancies. For $D_0$, the difference between the 6D+6D (Ref. [13]) and full 12D variational computations (Ref. [33]) is 2 $\mathrm{cm}^{-1}$ which in relative terms is even smaller than most of the discrepancies in the transition energies.

Our calculations with the WW19 PES give $D_0 = 1106$ $\mathrm{cm}^{-1}$, in excellent agreement with the experimental value of $1105 \pm 10$ $\mathrm{cm}^{-1}$ from Ref. [55]. However, we have to take into account that if monomer-flexibility effects were accounted for, this value would probably increase and would move away from the mean experimental value. If this shift is 5 $\mathrm{cm}^{-1}$, as in the case of the HBB2 PES, the resulting $D_0$ would be just slightly outside the experimental uncertainty interval. Needless to emphasize, the present agreement of theory with experiment to within 1 $\mathrm{cm}^{-1}$, or even the estimated agreement to within 6 $\mathrm{cm}^{-1}$ after the correction for monomer-flexibility effect, must be considered partly fortuitous due to uncertainties in *ab initio* interaction energies and those resulting from fitting. Since $D_0$ is directly related to $D_{\mathrm{e}}$, as shown above, one cannot expect agreement between experiment and theory better than about 10 $\mathrm{cm}^{-1}$ and even this requires some cancellation of errors. However, one can expect that the next generation of water dimer PESs should decrease theoretical uncertainties by nearly an order of magnitude (by removing the FC approximation in the case of WW19 PES, extending it to 12 dimensions, and improving the quality of the fit in this order). Then theory may again be able to challenge experiment on the dissociation energy of the water dimer.

TABLE XX. Binding, dissociation, and zero-point vibrational energies (in $cm^{-1}$) of $(H_2O)_2$.

| PES | Quantum nuclear motion[a] | | Monomer geometry[b] | $D_e$ | ZPVE[c] | $D_0$ | Reference |
|---|---|---|---|---|---|---|---|
| | Method | Dim. | | | | | |
| HBB1 | var | {6D} | $r^*_{eq}$ | 1656 | 658 | 998 | [10] |
| HBB1 | var | {6D} | $r_{eq}$ | 1648 | 655 | 993 | (present work) |
| HBB1 | var | {6D} | $\langle r \rangle_0$ | 1701 | 667 | 1034 | (present work) |
| HBB1 | DMC | {12D} | | 1666 | 624 | 1042 | [10] |
| HBB2 | var | {6D} | $r_{eq}$ | 1723 | 673 | 1050 | (present work) |
| HBB2 | var | {6D} | $\langle r \rangle_0$ | 1778 | 685 | 1093 | (present work) |
| HBB2 | var | {6D+6D} | | 1740[d] | 634 | 1096 | [34] |
| HBB2 | DMC | {12D} | | 1740[d] | 639±4 | 1103±4 | [12] |
| SAPT-5s | var | {6D} | $r_{GED}$ | 1700 | 633 | 1067 | [115] |
| CCpol-5s | var | {6D} | $r_{GED}$ | 1783 | 672 | 1111 | [8] |
| CCpol-8s | var | {6D} | $r_{GED}$ | 1785 | 691 | 1094 | [9] |
| CCpol-8sf | var | {6D+6D} | | 1755[d] | 667 | 1108 | [13] |
| CCpol-8sfIR | var | {12D} | | 1755 | 667 | 1110 | [33] |
| WW19 PES | var | {6D} | $\langle r \rangle_0$ | 1791 | 685 | 1106 | (present work) |
| State of the art value for $D_e$[e] | | | | 1755 | | | [57] |
| State of the art value for $D_e$[f] | | | | 1756 | | | [57] |
| Experiment | | | | | | 1256 | [114] |
| Experiment | | | | | | 1105±10 | [55] |

[a] Method used for the vibrational computations: variational (var) or diffusion Monte Carlo (DMC). Column "Dim." is the number of active vibrational degrees of freedom.

[b] Type of monomer geometry in reduced-dimensionality computations. Some of the rigid-monomer geometries, $r_{eq}$, $\langle r \rangle_0$ and $r_{GED}$, are given in Table II. The $r^*_{eq}$ is from Ref. [10].

[c] Only the intermolecular part of the ZPV energy is shown.

[d] Available from Refs. [12, 13] only to three significant digits.

[e] $D_e$ value at the nonrelativistic effects BO level to be compared with other $D_e$ values listed in the table with fully relaxed monomers ($\{6D + 6D\}$ or $\{12D\}$).

[f] As in footnote e, but including relativistic effects and the diagonal BO correction.

The results in Table XX also show that for systems for which a full-dimensional PES and/or full-dimensional nuclear-motion computations are not feasible (although full-dimensional DMC calculations can be done for very large systems), reduced-dimensionality PESs should give dissociation energies with an uncertainty on the order of 1%. For an even better accuracy, one could use a reduced-dimensionality PES obtained from a full-dimensional PES by averaging over intramonomer vibrations [53, 54, 80].

Table XXI summarizes the dissociation energies for the three dimers of water and methane computed in the present work. The fact that the binding energy of methane to water is larger than that of methane to methane might be counter-intuitive by remembering the organic chemistry wisdom: "similia similibus solvuntur" (like dissolves like) and the hydrophobicity of methane. However, the naive view that hydrophobicity is due to two hydrophobic molecules binding stronger to each other than to water is simply not true and in fact the effective interaction between such molecules dissolved in water (which results in hydrophobicity) is mediated by the network of water molecules [21].

Using the data in Table XXI, it is interesting to discuss the $D_0/D_e$ ratios: 0.62, 0.40, and 0.54 for $(H_2O)_2$, $CH_4{\cdot}H_2O$, $(CH_4)_2$, respectively. One would generally expect such ratios to decrease with the decrease of well depth (for example, in the extreme case of $^4He_2$, this ratio is 0.00015 [117]), but the value for $CH_4{\cdot}H_2O$ is too small. We believe that this is due to the presence of the secondary minimum ($D_e = 242$ cm$^{-1}$) and the very small barrier between the global and the secondary minima. The ground state of $CH_4{\cdot}H_2O$ is above the secondary minimum and its wave function penetrates into this region, which pushes this level up compared to where it would have been if the secondary minimum were not present.

TABLE XXI. Binding, dissociation, and ZPV energies obtained for the dimers of methane and water. The binding energy (depth of the PES) and the dissociation energy are both measured from the dissociation asymptote, whereas the zero-point vibrational energy (ZPVE) is measured from the global minimum value of the PES.

| | $(H_2O)_2$ | $CH_4{\cdot}H_2O$ | $(CH_4)_2$ |
|---|---|---|---|
| $D_e$ [cm$^{-1}$] | 1791 | 368 | 190 |
| ZPVE [cm$^{-1}$] | 685 | 219 | 86.6 |
| $D_0$ [cm$^{-1}$] | 1106 | 149 | 104 |
| $D_0$ [kcal mol$^{-1}$] | 3.162 | 0.426 | 0.297 |

## VI. SUMMARY AND CONCLUSIONS

Rigid-monomer PESs have been developed for the three molecular dimers that can be formed by the water and methane molecules. The surfaces are of the same functional form and are fitted to the same level of *ab initio* theory. Consequently, the PESs have a more-or-less uniform accuracy, although surfaces involving methane have somewhat lower relative accuracy due the use of a smaller number of off-atomic sites in the fitting functions for methane than for water. However, the absolute accuracy, important for modelling thermodynamic properties of the bulk phase and clathrates, is uniform. The level of *ab initio* theory and the form of the fitting function is on par with the best published PESs and the functional form is simple enough that the PESs developed could be used in MD investigations of clathrates or of bulk phases involving water and methane, leading to significantly improved predictions for such systems.

The PESs were developed in a fully automated fashion using the autoPES program package [44]. The spectroscopic vibrational intervals obtained show that the automated development provides PESs as accurate as developed "manually" with a large expense of human time and often with tailor-made adjustments for specific applications.

Two of the PESs developed in this work, WW19 and WM19 for $(H_2O)_2$ and $CH_4{\cdot}H_2O$, respectively, are validated by comparing vibrational vibrational states with experiment and with earlier theoretical results. No far-infrared spectra are available for $(CH_4)_2$ and the present work reports the first variational vibrational results based on an *ab initio* PES for this system, MM19. We find an excellent agreement with recently published theoretical and available experimental results for $(H_2O)_2$, despite the fact that our WW19 PES uses the rigid-monomer approximation. Clearly, this approximation, provided it uses monomers in their $\langle r \rangle_0$ geometries, works very well for the investigated dimers. It is interesting to note that the $D_0$ dissociation energy (an 'absolute quantity') is also obtained accurately (ca. 1 % uncertainty) within the rigid monomer-approximation using effective monomer structures.

While we discuss the three dimers together, they are, of course, very different—with about the one order of magnitude difference in the $D_\mathrm{e}$ values. This disparity initiated a study of relations between PES characteristics and (ro)vibrational quantum dynamical properties. A detailed account of rovibrational quantum dynamical results and their analysis will be reported in future work [101]. For the present study, we only point out that the vibrational splittings due to the feasible exchanges of permutation-inversion versions have very different characteristics for the three dimers. We think about not only the obvious increase in the order of the molecular symmetry group by going from $(H_2O)_2$ (16) through $CH_4{\cdot}H_2O$ (48) to $(CH_4)_2$ (576), and thereby giving rise to more abundant splittings, but it is the notion and identification of more or less isolated splitting patterns, and through them intermolecular vibrations, in the traditional sense. For the $(H_2O)_2$ dimer, it is possible to identify fairly clear splittings for at least six vibrational states. These six states are spread over a ca. 170 $\mathrm{cm}^{-1}$ with splittings spanning an energy range from 3 $\mathrm{cm}^{-1}$ to 60 $\mathrm{cm}^{-1}$ for the different vibrations, which is interesting when compared with the 1106 $\mathrm{cm}^{-1}$ $D_0$ value, the lowest barrier of 189 $\mathrm{cm}^{-1}$, and several barriers with heights around 200 $\mathrm{cm}^{-1}$. For $CH_4{\cdot}H_2O$, we could identify and separate the splitting manifold corresponding to the zero-point vibration of the global minimum, which is spread over ca. 35 $\mathrm{cm}^{-1}$, while its $D_0 = 149$ $\mathrm{cm}^{-1}$ and the lowest barrier is only 3.1 $\mathrm{cm}^{-1}$. It was also possible to identify the lower part of the splitting for the intermolecular stretching fundamental and the lowest energy states corresponding to the zero-point vibrational splitting of the secondary minimum. For the MM dimer, the 48-fold ($|G_{576}|/|D_{3\mathrm{d}}| = 48$) splitting of the zero-point vibration spans ca. 45 $\mathrm{cm}^{-1}$ and it overlaps with other splittings (to be discussed in detail in our future work [101]) including the intermolecular stretching fundamental band. In general, the identification of distinct intermolecular vibrations for $(CH_4)_2$, split up due to the feasible exchanges, is problematic. Its $D_0$ value is 104 $\mathrm{cm}^{-1}$, whereas the barriers start at 15.7 $\mathrm{cm}^{-1}$.

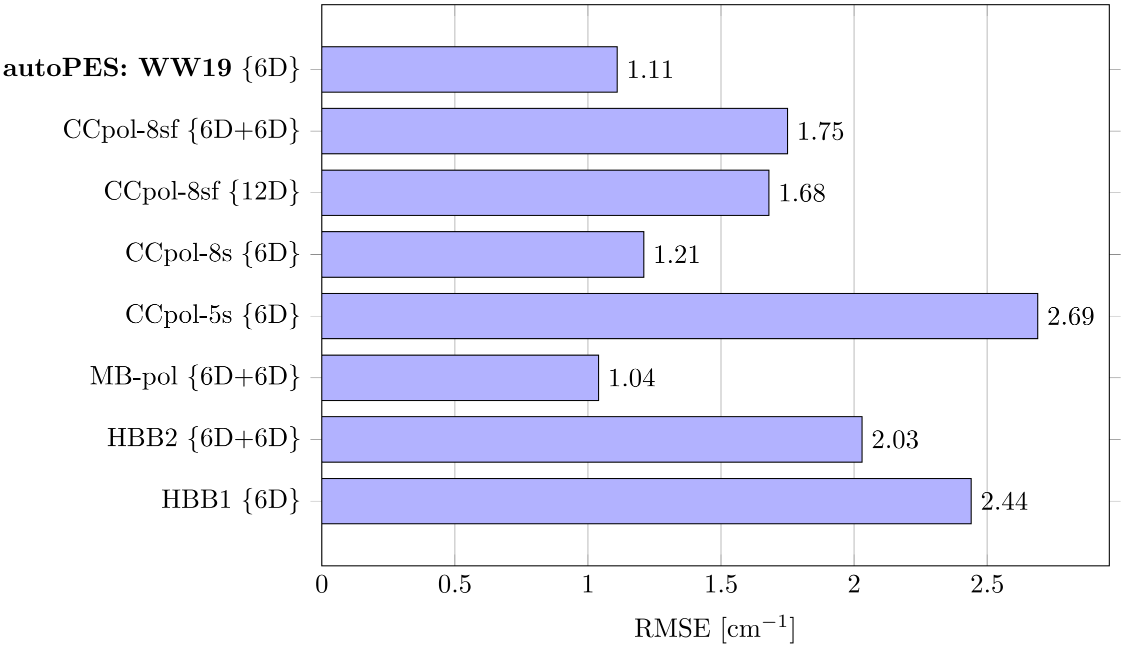

FIG. 2. Comparison of the accuracy of the *ab initio* $(H_2O)_2$ PESs: RMSEs of the variational vibrational transitions and splittings from experiment. The WW19 PES was developed in the present work. We indicate in the curly bracket after each PES the number of active vibrational degrees of freedoms in the variational vibrational computations. For a detailed comparison and references see Table XVII.

Along the $(H_2O)_2$, $CH_4{\cdot}H_2O$, $(CH_4)_2$ series, while the increase of the number of feasible permutation-inversion operations, *i.e.,* equivalent wells on the PESs separated with surmountable barriers, gives rise to richer symmetry properties, the lowering of the height of these barriers blurs the traditional notion of (large-amplitude, intermolecular) vibrational states, and approaches the limit of coupled quantum rotors [39], in which case the coupling due to their angular momenta becomes more important than the attraction by weak intermolecular interactions. Among the three dimers studied here, $(H_2O)_2$ is more on the tunneling splitting side of the scale and $(CH_4)_2$ is closer to the weakly interacting coupled-rotor picture. $CH_4{\cdot}H_2O$ is probably an intermediate case, and for which the presence of a secondary minimum structure, only ca. 126 cm$^{-1}$ higher in energy than the global minimum of the same point-group symmetry, makes the situation even more complicated. In particular, the dissociation energy of this dimer is much smaller than it could be expected based on the depth ($D_e$) of the PES valley.

Comparison with the high-resolution spectroscopic experiments for $(H_2O)_2$ allows a quantitative assessment of the accuracy of the newly-developed WW19 PES. A summary of the performance of the WW19 PES relative to the published results is given in Fig. 2. This figure shows that for the water dimer the WW19 PES performs very well, in fact together with the MB-pol PES it gives the smallest RMSE from experiment among all surfaces.

For the methane-water dimer, the available high-resolution far-infrared measurements correspond to rotational excitations within a vibrational band, for which rovibrational computations [38, 39] with the two earlier developed PESs [16, 17] gave excellent agreement. Concerning the vibrational intervals, however, for which there is not any available experimental information, the agreement between the three available PESs is not perfect, with the largest 2.3 (4.0) $\mathrm{cm}^{-1}$ deviation in transition energies for the lowest-energy species of the zero-point vibration of the global and that of the secondary minimum between the PES from Ref. [17] (Ref. [16]) and the WM19 PES.

For $(CH_4)_2$, the present work reports the variational vibrational states for the first time. We are not aware of any experimental results for the intermolecular bound states of this complex, although there are high-resolution experiments in the infrared spectral region [42, 43]. We expect that the MM19 PES (as well as the WM19 PES) should provide spectral transition similarly accurate as the WW19 PES since the three surfaces have been developed in the same procedure.

## Supplementary Information

The Supplementary Information contains the following material:

- **som.pdf:** Details about the form of the fitting function and the fitting procedures; geometric coordinates of minima; character table for group $G_{576}$; definition of SAPT corrections included in Table IV. This material cites Refs. [9, 20, 24, 44, 50, 58, 61, 111, 118–124].
- **ch4h2o_pes.f90:** Fortran program computing all surfaces for arbitrary water and methane clusters. The instructions on how to run this program are included as comments at the beginning of the program.
- **fit_inter.dat.*:** Parameters for a given PES except monomer geometries. See ch4h2o_pes.f90 for format specifications.
- ***_fit_report.txt:** Details of the fit including monomer geometries in three version: $\bar{r}$, $\langle r_{\mathrm{H}} \rangle_0$, and $\langle r_{\mathrm{D}} \rangle_0$. Users can construct any other geometry following the prescription in Sec. II B.
- **CH4-H2O-MD:** File with this string contains the parameters for the fit WM19-MD, the version of WM19 with partial charges consistent with WW19 and MM19, which is needed for MD simulations. All other parameters from WM19 were reoptimized without adding any new grid points and are not consistent with WW19 and MM19. The RMSE of this fit for $E_{\mathrm{int}} < 0$ is 0.022 kcal/mol, about twice as large as that of WM19, but completely adequate for MD simulations.

## Conflicts of interest

There are no conflicts of interest to declare.

**Acknowledgment**

The work of M.P.M. and K.S. has been supported by the U.S. Army Research Laboratory and the Army Research Office under Grant W911NF-13-1-0387 and by the National Science Foundation Grant CHE-1566036. The work performed by A.G.C. received support from NKFIH (grant no. K119658) and from the grant VEKOP-2.3.2-16-2017-00014. E.M. acknowledges financial support from a PROMYS Grant (no. IZ11Z0_166525) of the Swiss National Science Foundation.

[1] E. D. Sloan and C. A. Koh, *Clathrate Hydrates of Natural Gases, 3rd ed.* (CRC Press, Boca Raton, 2008).

[2] T. S. Collett, A. H. Johnson, C. C. Knapp, and R. Boswell, in *Natural Gas Hydrates: A Review*, Vol. M 89, edited by T. S. Collett, A. H. Johnson, C. C. Knapp, and R. Boswell (AAPG/NETL/AAPG Foundation/AAPG EMD, 2010) pp. 146–219.

[3] G. C. Groenenboom, E. M. Mas, R. Bukowski, K. Szalewicz, P. E. S. Wormer, and A. van der Avoird, Phys. Rev. Lett. **84**, 4072 (2000).

[4] R. Bukowski, K. Szalewicz, G. C. Groenenboom, and A. van der Avoird, J. Chem. Phys. **125**, 044301 (2006).

[5] K. Szalewicz, G. Murdachaew, R. Bukowski, O. Akin-Ojo, and C. Leforestier, in *Lecture Series on Computer and Computational Science: International Conference of Computational Methods in Science and Engineering (ICCMSE 2006)*, Vol. 6, edited by G. Maroulis and T. Simos (Brill Academic Publishers, Leiden, 2006) pp. 482–491.

[6] X. Huang, B. J. Braams, and J. M. Bowman, J. Phys. Chem. A **110**, 445 (2006).

[7] R. Bukowski, K. Szalewicz, G. C. Groenenboom, and A. van der Avoird, Science **315**, 1249 (2007).

[8] R. Bukowski, K. Szalewicz, G. C. Groenenboom, and A. van der Avoird, J. Chem. Phys. **128**, 094314 (2008).

[9] W. Cencek, K. Szalewicz, C. Leforestier, R. van Harrevelt, and A. van der Avoird, Phys. Chem. Chem. Phys. **10**, 4716 (2008).

[10] X. Huang, B. J. Braams, J. M. Bowman, R. E. A. Kelly, J. Tennyson, G. C. Groenenboom, and A. van der Avoird, J. Chem. Phys. **128**, 034312 (2008).

[11] K. Szalewicz, C. Leforestier, and A. van der Avoird, Chem. Phys. Lett. **482**, 1 (2009).

[12] A. Shank, Y. Wang, A. Kaledin, B. J. Braams, and J. M. Bowman, J. Chem. Phys. **130**, 144314 (2009).

[13] C. Leforestier, K. Szalewicz, and A. van der Avoird, J. Chem. Phys. **137**, 014305 (2012).

[14] V. Babin, C. Leforestier, and F. Paesani, J. Chem. Theory Comp. **9**, 5395 (2013).

[15] P. Jankowski, G. Murdachaew, R. Bukowski, O. Akin-Ojo, C. Leforestier, and K. Szalewicz, J. Phys. Chem. A **119**, 2940 (2015).

[16] O. Akin-Ojo and K. Szalewicz, J. Chem. Phys. **123**, 134311 (2005).

[17] C. Qu, R. Conte, P. L. Houston, and J. M. Bowman, Phys. Chem. Chem. Phys. **17**, 8172 (2015).

[18] R. Hellmann, E. Bich, and E. Vogel, J. Chem. Phys. **128**, 214303 (2008).

[19] G. Garberoglio, P. Jankowski, K. Szalewicz, and A. H. Harvey, Farad. Disc. **212**, 467 (2018).

[20] U. Góra, W. Cencek, R. Podeszwa, A. van der Avoird, and K. Szalewicz, J. Chem. Phys. **140**, 194101 (2014).

[21] O. Akin-Ojo and K. Szalewicz, J. Chem. Phys. **150**, 084501 (2019).

[22] J. G. McDaniel and A. Yethiraj, J. Chem. Phys. **144**, 137101 (2016).

[23] K. Szalewicz, R. Bukowski, and B. Jeziorski, in *Theory and Applications of Computational Chemistry: The First 40 Years. A Volume of Technical and Historical Perspectives*, edited by C. E. Dykstra, G. Frenking, K. S. Kim, and G. E. Scuseria (Elsevier, Amsterdam, 2005) Chap. 33, pp. 919–962.

[24] O. Akin-Ojo and K. Szalewicz, J. Chem. Phys. **138**, 024316 (2013).

[25] E. Arunan, G. R. Desiraju, R. A. Klein, J. Sadlej, S. Scheiner, I. Alkorta, D. C. Clary, R. H. Crabtree, J. J. Dannenberg, P. Hobza, H. G. Kjaergaard, A. C. Legon, B. Mennucci, and D. J. Nesbitt, Pure Appl. Chem. **83**, 1637 (2011).

[26] J. Hoja, A. F. Sax, and K. Szalewicz, Chem. Europ. J. **20**, 2292 (2014).

[27] S. C. Althorpe and D. C. Clary, J. Chem. Phys. **101**, 3603 (1994).

[28] S. C. Althorpe and D. C. Clary, J. Chem. Phys. **102**, 4390 (1995).

[29] R. S. Fellers, C. Leforestier, L. B. Braly, M. G. Brown, and R. J. Saykally, Science **284**, 945 (1999).

[30] R. S. Fellers, L. B. Braly, R. J. Saykally, and C. Leforestier, J. Chem. Phys. **110**, 6306 (1999).

[31] F. N. Keutsch, L. B. Braly, M. G. Brown, H. A. Harker, P. B. Petersen, C. Leforestier, and R. J. Saykally, J. Chem. Phys. **119**, 8927 (2003).

[32] F. N. Keutsh, N. Goldman, H. A. Harker, C. Leforestier, and R. J. Saykally, Mol. Phys. **101**, 3477 (2003).

[33] X.-G. Wang and T. Carrington, Jr., J. Chem. Phys. **148**, 074108 (2018).

[34] C. Leforestier, Phil. Trans. R. Soc. A **370**, 2675 (2012).

[35] A. Mukhopadhyay, W. T. Cole, and R. J. Saykally, Chem. Phys. Lett. **633**, 13 (2015).

[36] L. Dore, R. C. Cohen, C. A. Schmuttenmaer, K. L. Busarow, M. J. Elrod, J. G. Loeser, and R. J. Saykally, J. Chem. Phys. **100**, 863 (1994).

[37] R. D. Suenram, G. T. Fraser, F. J. Lovas, and Y. Kawashima, J. Chem. Phys. **101**, 7230 (1994).

[38] J. Sarka, A. G. Csaszar, S. C. Althorpe, D. J. Wales, and E. Matyus, Phys. Chem. Chem. Phys. **18**, 22816 (2016).

[39] J. Sarka, A. G. Csaszar, and E. Matyus, Phys. Chem. Chem. Phys. **19**, 15335 (2017).

[40] S. Tsuzuki, T. Uchimaru, K. Tanabe, and S. Kuwajima, J. Phys. Chem. **98**, 1830 (1994).

[41] A. H. T. Li and S. D. Chao, J. Chinese Chem. Soc. **63**, 282 (2016).

[42] A. Hamdan, Infrared Spectroscopy of Methane Dimer, PhD Dissertation, Ruhr-Universität Bochum, 2005.

[43] H. Hoshina, D. Skvortsov, M. N. Slipchenko, B. G. Sartakov, and A. F. Vilesov, J. Chem. Phys. **143**, 084305 (2015).

[44] M. P. Metz, K. Piszczatowski, and K. Szalewicz, J. Chem. Theory Comput. **12**, 5895 (2016).

[45] V. Babin, G. R. Medders, and F. Paesani, J. Phys. Chem. Lett. **3**, 3765 (2012).

[46] G. R. Medders, V. Babin, and F. Paesani, J. Chem. Theory Comput. **9**, 1103 (2013).

[47] C. Millot and A. J. Stone, Mol. Phys. **77**, 439 (1992).

[48] E. M. Mas, K. Szalewicz, R. Bukowski, and B. Jeziorski, J. Chem. Phys. **107**, 4207 (1997).

[49] C. Millot, J. C. Soetens, M. T. C. M. Costa, M. P. Hodges, and A. J. Stone, J. Phys. Chem. A **102**, 754 (1998).

[50] E. M. Mas, R. Bukowski, K. Szalewicz, G. C. Groenenboom, P. E. S. Wormer, and A. van der Avoird, J. Chem. Phys. **113**, 6687 (2000).

[51] M. J. Smit, G. C. Groenenboom, P. E. S. Wormer, A. van der Avoird, R. Bukowski, and K. Szalewicz, J. Phys. Chem. A **105**, 6212 (2001).

[52] K. Szalewicz, S. J. Cole, W. Kolos, and R. J. Bartlett, J. Chem. Phys. **89**, 3662 (1988).

[53] P. Jankowski, A. R. W. McKellar, and K. Szalewicz, Science **336**, 1147 (2012).

[54] P. Jankowski, L. A. Surin, A. Potapov, S. Schlemmer, A. R. W. McKellar, and K. Szalewicz, J. Chem. Phys. **138**, 084307 (2013).

[55] B. E. Rocher-Casterline, L. C. Ch'ng, A. K. Mollner, and H. Reisler, J. Chem. Phys. **134**, 211101 (2011).

[56] L. C. Ch'ng, A. K. Samanta, G. Czako, J. M. Bowman, and H. Reisler, J. Am. Chem. Soc. **134**, 15430 (2012).

[57] J. R. Lane, J. Chem. Theory Comput. **9**, 316 (2013).

[58] R. Bukowski, K. Szalewicz, G. C. Groenenboom, and A. van der Avoird, J. Chem. Phys. **128**, 094313 (2008).

[59] R. A. Kendall, T. H. Dunning Jr, and R. J. Harrison, J. Chem. Phys. **96**, 6796 (1992).

[60] H. L. Williams, E. M. Mas, K. Szalewicz, and B. Jeziorski, J. Chem. Phys. **103**, 7374 (1995).

[61] M. P. Metz, K. Piszczatowski, and K. Szalewicz, "*autoPES: Automatic Intermolecular Potential Energy Surface Generation Software*," `http://www.physics.udel.edu/~szalewic/SAPT/index.html` (2016).

[62] S. F. Boys and F. Bernardi, Mol. Phys. **19**, 553 (1970).

[63] T. Helgaker, W. Klopper, H. Koch, and J. Noga, J. Chem. Phys. **106**, 9639 (1997).

[64] O. Akin-Ojo, R. Bukowski, and K. Szalewicz, J. Chem. Phys. **119**, 8379 (2003).

[65] R. Podeszwa, R. Bukowski, and K. Szalewicz, J. Chem. Theo. Comp. **2**, 400 (2006).

[66] A. J. Stone, *The Theory of Intermolecular Forces*, 2nd ed. (Clarendon Press, Oxford, 2013).

[67] B. Jeziorski, R. Moszyński, and K. Szalewicz, Chem. Rev. **94**, 1887 (1994).

[68] J. P. Perdew, K. Burke, and M. Ernzerhof, Phys. Rev. Lett. **77**, 3865 (1996).

[69] C. Adamo and V. Barone, J. Chem. Phys. **110**, 6158 (1999).

[70] M. Grüning, O. V. Gritsenko, S. J. A. van Gisbergen, and E. J. Baerends, J. Chem. Phys. **114**, 652 (2001).

[71] H. L. Williams and C. F. Chabalowski, J. Phys. Chem. A **105**, 646 (2001).

[72] A. J. Misquitta and K. Szalewicz, Chem. Phys. Lett. **357**, 301 (2002).

[73] A. Heßelmann and G. Jansen, Chem. Phys. Lett. **357**, 464 (2002).

[74] A. Heßelmann and G. Jansen, Chem. Phys. Lett. **362**, 319 (2002).

[75] A. J. Misquitta, B. Jeziorski, and K. Szalewicz, Phys. Rev. Lett. **91**, 033201 (2003).

[76] A. Heßelmann and G. Jansen, Chem. Phys. Lett. **367**, 778 (2003).

[77] A. J. Misquitta and K. Szalewicz, J. Chem. Phys. **122**, 214109 (2005).

[78] A. J. Misquitta, R. Podeszwa, B. Jeziorski, and K. Szalewicz, J. Chem. Phys. **123**, 214103 (2005).

[79] A. Hesselmann, G. Jansen, and M. Schütz, J. Chem. Phys. **122**, 014103 (2005).

[80] M. Jeziorska, P. Jankowski, K. Szalewicz, and B. Jeziorski, J. Chem. Phys. **113**, 2957 (2000).

[81] E. M. Mas and K. Szalewicz, J. Chem. Phys. **104**, 7606 (1996).

[82] G. Czakó, E. Mátyus, and A. G. Császár, J. Phys. Chem. A **113**, 11665 (2009).

[83] O. L. Polyansky, A. G. Csaszar, S. V. Shirin, N. F. Zobov, P. Barletta, J. Tennyson, D. W. Schwenke, and P. J. Knowles, Science **299**, 539 (2003).

[84] P. Barletta, S. V. Shirin, N. F. Zobov, O. L. Polyansky, J. Tennyson, E. F. Valeev, and A. G. Csaszar, J. Chem. Phys. **125**, 204307 (2006).

[85] A. G. Csaszar, G. Czaka, T. Furtenbacher, J. Tennyson, V. Szalay, S. V. Shirin, N. F. Zobov, and O. L. Polyansky, J. Chem. Phys. **122**, 214305 (2005).

[86] D. W. Schwenke and H. Partridge, Spectrochim. Acta A **57**, 887 (2001).

[87] K. Kuchitsu and L. S. Bartell, J. Chem. Phys. **36**, 2460 (1962).

[88] M. Nakata and K. Kuchitsu, J. Chem. Soc. Jpn. **null**, 1446 (1986).

[89] A. Owens, S. N. Yurchenko, A. Yachmenev, J. Tennyson, and W. Thiel, J. Chem. Phys. **145**, 104305 (2016).

[90] G. Murdachaew and K. Szalewicz, Faraday Discuss. **118**, 121 (2001).

[91] G. Murdachaew, R. Bukowski, and K. Szalewicz, Phys. Rev. Lett. **88**, 123202 (2002).

[92] K. Szalewicz, Wiley Interdis. Rev.: Comp. Mol. Sci. **2**, 254 (2012).

[93] J. A. Odutola and T. R. Dyke, J. Chem. Phys. **72**, 5062 (1980).

[94] G. S. Tschumper, M. L. Leininger, B. C. Hoffman, E. F. Valeev, H. F. Schaefer III, and M. Quack, J. Chem. Phys. **116**, 690 (2002).

[95] T. B. Adler, G. Knizia, and H.-J. Werner, J. Chem. Phys. **127**, 221106 (2007).

[96] B. J. Smith, D. J. Swanton, J. A. Pople, and H. F. Schaefer III, J. Chem. Phys. **92**, 1240 (1990).

[97] H. I. Rivera-Arrieta, J. M. Turney, and H. F. Schaefer, III, J. Chem. Theory Comput. **13**, 1478 (2017).

[98] A. van der Avoird, R. Podeszwa, K. Szalewicz, C. Leforestier, R. van Harrevelt, P. R. Bunker, M. Schnell, G. von Helden, and G. Meijer, Phys. Chem. Chem. Phys. **12**, 8219 (2010).

[99] E. Mátyus, G. Czakó, and A. G. Császár, J. Chem. Phys. **130**, 134112 (2009).

[100] C. Fábri, E. Mátyus, and A. G. Császár, J. Chem. Phys. **134**, 074105 (2011).

[101] "Paper II: Rovibrational states for the three dimers and their detailed analysis." (2019).

[102] E. Mátyus, J. Simunek, and A. G. Császár, J. Chem. Phys. **131**, 074106 (2009).

[103] H. Wei and T. Carrington, Jr., J. Chem. Phys. **97**, 3029 (1992).

[104] J. Echave and D. C. Clary, Chem. Phys. Lett. **190**, 225 (1992).

[105] T. R. Dyke, J. Chem. Phys. **66**, 492 (1977).

[106] G. T. Fraser, Int. Rev. Phys. Chem. **10**, 189 (1991).

[107] E. Zwart, J. J. ter Meulen, W. Leo Meerts, and L. H. Coudert, J. Mol. Spectrosc. **147**, 27 (1991).

[108] L. B. Braly, K. Liu, M. G. Brown, F. N. Keutsch, R. S. Fellers, and R. J. Saykally, J. Chem. Phys. **112**, 10314 (2000).

[109] G. Czakó, E. Mátyus, and A. G. Császár, J. Phys. Chem. A **113**, 11665 (2009).

[110] J. Odutola, D. L. Alvis, C. W. Curtis, and T. R. Dyke, Mol. Phys. **42**, 267 (1981).

[111] R. Schmied and K. Lehmann, J. Mol. Spectrosc. **226**, 201 (2004).

[112] The GAP Group, GAP – Groups, Algorithms, and Programming, Version 4.8.10; 2018. (https://www.gap-system.org).

[113] P. R. Bunker and P. Jensen, *Molecular symmetry and spectroscopy, 2nd Edition* (NRC Research Press, Ottawa, 1998).

[114] L. A. Curtiss, D. J. Frurip, and M. Blander, J. Chem. Phys. **71**, 2703 (1979).

[115] G. C. Groenenboom, P. E. S. Wormer, A. van der Avoird, E. M. Mas, R. Bukowski, and K. Szalewicz, J. Chem. Phys. **113**, 6702 (2000).

[116] C. Leforestier, F. Gatti, R. Fellers, and R. Saykally, J. Chem. Phys. **117**, 8710 (2002).

[117] M. Przybytek, W. Cencek, B. Jeziorski, and K. Szalewicz, Phys. Rev. Lett. **119**, 123401 (2017).

[118] W. L. Jorgensen, D. S. Maxwell, and J. Tirado-Rives, J. Am. Chem. Soc. **118**, 11225 (1996).

[119] K. T. Tang and J. P. Toennies, J. Chem. Phys. **80**, 3726 (1984).

[120] U. Gora, R. Podeszwa, W. Cencek, and K. Szalewicz, J. Chem. Phys. **135**, 224102 (2011).

[121] W. F. Murphy, J. Chem. Phys. **67**, 5877 (1977).

[122] H. Watson and K. Ramaswamy, Proc. Royal Soc. London A: Math., Phys. and Eng. Sci. **156**, 144 (1936).

[123] F. Rob and K. Szalewicz, Chem. Phys. Lett. **572**, 146 (2013).

[124] F. Rob and K. Szalewicz, Mol. Phys. **111**, 1430 (2013).